



MOX-Report No. 66/2021

**On mathematical and numerical modelling of
multiphysics wave propagation with polygonal
Discontinuous Galerkin methods**

Antonietti, P.F.; Botti, M.; Mazzieri, I.

MOX, Dipartimento di Matematica
Politecnico di Milano, Via Bonardi 9 - 20133 Milano (Italy)

mox-dmat@polimi.it

<http://mox.polimi.it>

On mathematical and numerical modelling of multiphysics wave propagation with polygonal Discontinuous Galerkin methods *

Paola F. Antonietti, Michele Botti, Ilario Mazzieri

Abstract

In this work we present discontinuous Galerkin finite element methods on polytopal grids (PolydG) for the numerical simulation of multiphysics wave propagation phenomena in heterogeneous media. In particular, we address wave phenomena in elastic, poro-elastic, and poro-elasto-acoustic materials. Wave propagation is modeled by using either the elastodynamics equation, in the elastic domain, the acoustics equations in the acoustic domain and the low-frequency Biot's equations in the poro-elastic one. The coupling between different models is realized by means of (physically consistent) transmission conditions, weakly imposed on the interface between the domains. For all models configuration, we introduce and analyse the PolydG semi-discrete formulation, which is then coupled with suitable time marching schemes. For the semi-discrete problem, we present the stability analysis and derive a-priori error estimates in a suitable energy norm. A wide set of verification tests with manufactured solutions are presented in order to validate the error analysis. Examples of physical interest are also shown to demonstrate the capability of the proposed methods.

Keywords: poroelasticity; acoustics; discontinuous Galerkin method; polygonal and polyhedral meshes; stability and convergence analysis

AMS subject classifications. 35L05, 65M12, 65M60, 74F10

1 Introduction

Multiphysics wave propagation in heterogeneous media is a very attractive research topic and, in recent decades, it has registered considerable interest in the mathematical, geophysical and engineering communities. Mathematical models for wave propagation phenomena range from the linear transport equation, to

*This work has received funding from the European Union's Horizon 2020 research and innovation programme under the Marie Skłodowska-Curie grant agreement no. 896616 (project PDGeoFF: Polyhedral Discretisation Methods for Geomechanical Simulation of Faults and Fractures in Poroelastic Media). The authors are members of the INdAM Research group GNCS and this work is partially funded by INdAM-GNCS. PFA has been partially funded by the research project PRIN n. 201744KLJL funded by MIUR.

the non-linear system of Navier-Stokes equations and they appear in many different scientific disciplines, such as acoustic engineering [1], vibroacoustics [2], aeronautical engineering, [3], in biomedical engineering [4], and computational geosciences, see [5] for a comprehensive review.

Thanks to the ongoing development of increasingly advanced high-performance computing facilities, the use of mathematical algorithms and numerical simulations for the solution of wave propagation problems has given a notable impulse towards a deeper understanding of these phenomena. Numerical methods designed for wave simulations must account for the following three distinguishing features: *accuracy*, *geometric flexibility* and *scalability*. *Accuracy* is essential to correctly reproduce the physical phenomenon, and allows to minimize numerical dispersion and dissipation errors that would deteriorate the quality of the solution. *Geometric flexibility* is required since the computational domain usually features complicated geometrical shapes as well as sharp media contrasts. *Scalability* is demanded to solve on parallel machines real computational models featuring several hundred of millions or even billions of unknowns.

In this work we will consider wave propagation problems arising from geophysics and we will analyze several models, with increasing complexity, employed in this scientific area. We will first present models of elastodynamics, then of poro-elasticity, and finally coupled poro-elasto-acoustics models.

Elastodynamic and viscoelastodynamic models are typically used for studying seismic waves that propagate across the globe and are generated by earthquakes, volcanic activity, or artificial explosions. As far as the elastodynamic equations are concerned, the most used numerical methods are finite differences [6, 7, 8], finite elements [9], finite volumes [10, 11, 12, 13], and spectral elements in either the conforming [14, 15, 16] or discontinuous setting [17, 18, 19].

Poro-elastodynamic models are used to describe the propagation of pressure and elastic waves through a porous medium. Pressure waves propagate through the saturating fluid inside pores, while elastic ones through the porous skeleton. In the pioneering work by Biot [20] general equations of waves propagation in poro-elastic materials were introduced. More recently, in [21] it is proposed a model of seismic waves in saturated soils, distinguishing in-phase (*fast*) movements between solid and fluid from out-phase (*slow*) ones. Poro-elasto-acoustic problem model acoustic/sound waves impacting a porous material and consequently propagating through it. The coupling between acoustic and poro-elastic domains, realized by means of physically consistent transmission conditions at the interface, is discussed in [22] and [23].

There is a wide strand of literature concerning the numerical discretization of poroelastic or poro-elasto-acoustic models. Here, we recall, e.g., the Lagrange Multipliers method [24, 25, 26], the finite element method [27, 28] the spectral and pseudo-spectral element method [29, 30], the ADER scheme [31, 23], the finite difference method [32], and references therein.

The aim of this work is to introduce and analyze a discontinuous Galerkin method on polygonal/polyhedral grids (PolydG) for the numerical discretization of multiphysics waves propagation through heterogeneous materials. The geometric flexibility and the arbitrary-order accuracy featured by the proposed

scheme are crucial within this context as they ensure at the same time the possibility of handling complex geometries and an intrinsic high-level of precision that are necessary to correctly represent the solutions.

For early results in the field of dG methods we refer the reader to [33, 34, 35, 36, 37, 38, 39] for second-order elliptic problems, to [40] for parabolic differential equations, to [41] for flows in fractured porous media, and to [42] for fluid structure interaction problems. In the framework of dG methods for hyperbolic problems, we mention [43, 44] for scalar wave equations on simplicial grids and the more recent PolydG discretizations designed in [45] for elastodynamics problems, in [46] for non-linear sound waves, in [47, 48] for coupled elasto-acoustic problems, and in [49] for poro-elasto-acoustic wave propagation.

The remaining part of the paper is structured as follows: in Section 2 we review differential models for wave propagation in heterogeneous Earth's media while in Section 3 we define the discrete setting used in the paper. The elastodynamic model and its numerical discretization through a PolydG method is recalled in Section 4, while Sections 5 and 6 discuss the numerical analysis of a PolydG method for wave propagation problems in poro-elastic and coupled poro-elastic-acoustic media, respectively. Different numerical tests of physical interest are introduced and discussed in Section 7. Finally, in Section 8 we draw some conclusions and discuss some perspective about future work.

Notation

In the following, for an open, bounded domain $D \subset \mathbb{R}^d$, $d = 2, 3$, the notation $\mathbf{L}^2(D)$ is used in place of $[L^2(D)]^d$, with $d \in \{2, 3\}$. The scalar product in $L^2(D)$ is denoted by $(\cdot, \cdot)_D$, with associated norm $\|\cdot\|_D$. Similarly, $\mathbf{H}^\ell(D)$ is defined as $[H^\ell(D)]^d$, with $\ell \geq 0$, equipped with the norm $\|\cdot\|_{\ell, D}$, assuming conventionally that $\mathbf{H}^0(D) \equiv \mathbf{L}^2(D)$. In addition we will use $\mathbf{H}(\text{div}, D)$ to denote the space of $\mathbf{L}^2(D)$ functions with square integrable divergence. In order to take into account essential boundary conditions, we also introduce the subspaces

$$H_0^1(D) = \{\psi \in H^1(D) \mid \psi|_{\Gamma_D} = 0\}, \quad (1)$$

$$\mathbf{H}_0^1(D) = \{\mathbf{v} \in \mathbf{H}^1(D) \mid \mathbf{v}|_{\Gamma_D} = \mathbf{0}\}, \quad (2)$$

$$\mathbf{H}_0(\text{div}, D) = \{\mathbf{z} \in \mathbf{H}(\text{div}, D) \mid (\mathbf{z} \cdot \mathbf{n}_p)|_{\Gamma_D} = 0\}, \quad (3)$$

with $\Gamma_D \subset \partial D$ having strictly positive Hausdorff measure. Given $k \in \mathbb{N}$ and a Hilbert space \mathbb{H} , the usual notation $C^k([0, T]; \mathbb{H})$ is adopted for the space of \mathbb{H} -valued functions, k -times continuously differentiable in $[0, T]$. The notation $x \lesssim y$ stands for $x \leq Cy$, with $C > 0$, independent of the discretization parameters, but possibly dependent on physical coefficients and the final time T .

2 Modelling seismic waves

A seismic event is the result of a sudden release of energy due to the rupture of a more fragile part of the Earth's crust called the fault. The deformation energy,

accumulated for tens and sometimes hundreds of years along the fault, is transformed into kinetic energy that radiates, in the form of waves, in all directions through the layers of the Earth. Seismic waves are therefore energy waves that produce an oscillatory movement of the ground during their passage. Seismic waves are subdivided into two main categories: volume waves and surface waves. The former are separate into compression waves (P) and shear waves (S). The faster P waves are transmitted both in liquids and in solids, while the slower S waves travel only in solid media. P waves induce ground motion aligned with the wave field direction while S waves induce ground motion perpendicular to the wave propagation field.

More and more frequently mathematical models are used for the study and analysis of ground motion. The solution of these models through appropriate numerical methods can quickly provide important information for the evaluation of the seismic hazard of a given region and for the planning of the territory in order to limit the socio-economic losses linked to the seismic event. In the following we consider the differential model that aims at describing the propagation of seismic wave within the Earth's media.

Let Ω be a bounded domain modeling the portion of the Earth where the passage of seismic waves occurs, and let its boundary $\partial\Omega$ be decomposed into three disjoint parts Γ_D , Γ_N and Γ_A , where the values of the displacement (Dirichlet conditions), the values of tractions (Neumann conditions), and the values of fictitious tractions (absorbing conditions) are imposed, respectively. For a temporal interval $(0, T]$, with $T > 0$, the equation governing the displacement field $\mathbf{u}(\mathbf{x}, t)$ of a dynamically disturbed elastic medium can be expressed as

$$\rho \partial_{tt} \mathbf{u} - \nabla \cdot \boldsymbol{\sigma} = \mathbf{f} \quad \text{in } \Omega \times (0, T], \quad (4)$$

where ρ is the mass density, \mathbf{f} define a suitable seismic source and $\boldsymbol{\sigma}$ is the stress tensor that models the constitutive behaviour of the material. Possible definition for $\boldsymbol{\sigma}$ and \mathbf{f} will be discussed in the sequel. Equation (4) is completed by prescribing suitable boundary conditions as well as initial conditions. For the latter, by choosing $\mathbf{u}(\cdot, 0) = \partial_t \mathbf{u}(\cdot, 0) = \mathbf{0}$, we suppose the domain to be at rest at the initial observation time.

2.1 Seismic waves in viscoelastic media

As we said previously, the stress tensor $\boldsymbol{\sigma}$ can be defined in different ways to properly model the behavior of the soil. Before presenting the main constitutive laws that can adopted for seismic wave propagation analysis we introduce: (i) the strain tensor $\boldsymbol{\epsilon}$ defined as the symmetric gradient, i.e., $\boldsymbol{\epsilon}(\mathbf{u}) = (\nabla \mathbf{u} + \nabla^T \mathbf{u})/2$, and (ii) the fourth-order (symmetric and positive definite) stiffness tensor \mathbb{D} , encoding the mechanical properties of the medium expressed in term of the first and the second Lamé coefficients, namely λ and μ , respectively. For an elastic material the generalized Hooke's law

$$\boldsymbol{\sigma} = \mathbb{D} : \boldsymbol{\epsilon} \quad (5)$$

defines the most general linear relation among all the components of the stress and strain tensor. In the most general case, i.e. a fully anisotropic material, equation (5) contains 21 material parameters. However in our case, i.e., for a perfectly isotropic material, (5) can be reduced as

$$\boldsymbol{\sigma}(\mathbf{u}) = \lambda \nabla \cdot \boldsymbol{\epsilon}(\mathbf{u}) \mathbf{I} + 2\mu \boldsymbol{\epsilon}(\mathbf{u}), \quad (6)$$

where \mathbf{I} is the identity tensor.

Pure elastic constitutive laws are not physically representative in the field of application of interest. A first model for visco-elastic media can be handled by modifying the equation of motion according to [50]. In the approach, the inertial term $\rho \partial_{tt} \mathbf{u}$ in (4) is replaced by $\rho \partial_{tt} \mathbf{u} + 2\rho\zeta \partial_t \mathbf{u} + \rho\zeta^2 \mathbf{u}$ where ζ is an attenuation parameter. As a matter of fact, with this substitution, i.e.,

$$\rho \partial_{tt} \mathbf{u} + 2\rho\zeta \partial_t \mathbf{u} + \rho\zeta^2 \mathbf{u} - \nabla \cdot \boldsymbol{\sigma} = \mathbf{f} \quad \text{in } \Omega \times (0, T], \quad (7)$$

all frequency components are equally attenuated with distance, resulting in a frequency proportional quality factor $Q \propto Q_0 \frac{f}{\alpha}$, with $Q_0 > 0$ and $\alpha \approx 1$ [51]. A second attenuation model, is obtained by considering materials “endowed with memory” in the sense that the state of stress at the instant t depends on all the deformations undergone by the material in previous times. This behaviour can be expressed through an integral equation of the form

$$\boldsymbol{\sigma}(t) = \int_0^t \frac{\partial \mathbb{D}}{\partial t}(t-s) : \boldsymbol{\epsilon}(s) ds \quad (8)$$

where the stress $\boldsymbol{\sigma}$ is determined by the entire strain history. Implicit in this law is the dependence on time of the Lamé parameters λ and μ , cf. [52, 53]. We remark that, by using (8) it is possible to obtain an almost constant quality factor Q in a suitable frequency range, cf. [53].

On $\partial\Omega$ several conditions can be set to correctly define the interaction between the wave and the domain boundary. Dirichlet conditions, are employed to prescribe the behaviour of the displacement field i.e. $\mathbf{u} = \mathbf{g}_D$, while Neumann conditions $\boldsymbol{\sigma} \mathbf{n} = \mathbf{g}_N$, where \mathbf{g}_N represents a distribution of surface load. Here \mathbf{n} denotes the outward pointing normal unit vector with respect to $\partial\Omega$.

For geophysical applications, since the domain of interest Ω represents a portion of the Earth the following boundary conditions are commonly adopted: (i) free-surface condition, i.e. $\boldsymbol{\sigma} \mathbf{n} = \mathbf{0}$ for the top Earth’s surface and (ii) transparent boundary conditions $\boldsymbol{\sigma} \mathbf{n} = \mathbf{t}$ for the remaining lateral and bottom surfaces. The latter consists in modeling the absorbing boundary layers by introducing a fictitious traction term $\mathbf{t} = \mathbf{t}(\mathbf{u}, \partial_t \mathbf{u})$, consisting of a linear combination of displacement space and time derivatives. Examples can be found in [54, 55]. In Figure 1 we report an illustrative example of domain Ω together with boundary conditions.

2.2 Seismic waves in porous media

Modeling wave propagation through fluid-saturated porous rock is crucial for the characterization of the seismic response of geologic formations. In this case, the

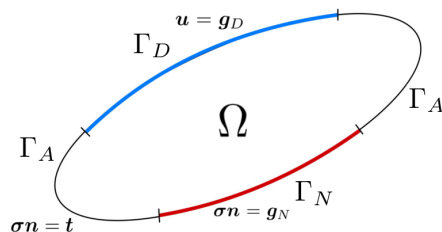


Fig. 1: Example of domain Ω with boundary $\partial\Omega$ divided into a Dirichlet Γ_D , a Neumann Γ_N and an absorbing Γ_A part.

effects arising from the interaction between the viscous fluid and the solid matrix have to be taken into account. In the framework of Biot's poro-elasticity theory [56, 20], the total stress tensor $\tilde{\sigma}$ additionally depends on the pore pressure p according to the following relation

$$\tilde{\sigma}(\mathbf{u}, p) = \boldsymbol{\sigma}(\mathbf{u}) - \beta p \mathbf{I}, \quad (9)$$

with $\boldsymbol{\sigma}(\mathbf{u})$ defined in (6) and $0 < \beta \leq 1$ denoting the Biot coefficient. Adding to the momentum balance equation (4) the inertial term corresponding to the filtration displacement $\mathbf{w} = \phi(\mathbf{w}_f - \mathbf{u})$, where $\phi > 0$ is the reference porosity and \mathbf{w}_f the fluid displacement, leads to

$$\rho \partial_{tt} \mathbf{u} + \rho_f \partial_{tt} \mathbf{w} - \nabla \cdot \tilde{\boldsymbol{\sigma}} = \mathbf{f} \quad \text{in } \Omega \times (0, T]. \quad (10)$$

Here, the average density ρ is given by $\rho = \phi \rho_f + (1 - \phi) \rho_s$, where $\rho_f > 0$ is the saturating fluid density and $\rho_s > 0$ is the solid density. To derive Biot's wave equations in Section 5, the rheology of the porous material (9) and the momentum balance (10) are combined with the dynamics of the fluid system described by Darcy's law and the conservation of fluid mass in the pores.

Two major differences have been observed when dealing with poro-elastic media instead of elastic ones: (i) the attenuation due to wave-induced fluid flow and (ii) the presence of an additional compressional wave of the second kind (slow P-wave), which becomes a diffusive mode in the low-frequency range, cf. [5]. As observed in [31], this slow P-wave is mainly localized near the material heterogeneities or the source.

2.3 Modelling the seismic source

Seismic wave can be generated by different natural and artificial sources. Depending on the problem's configuration one can consider a single point-source, an incidence of a plane wave or a finite-size rupturing fault.

We can define a point-wise force \mathbf{f} acting on a point \mathbf{x}_0 in the i^{th} direction as

$$\mathbf{f}(\mathbf{x}, t) = f(t) \mathbf{e}_i \delta(\mathbf{x} - \mathbf{x}_0), \quad (11)$$

where \mathbf{e}_i is the unit vector of the i^{th} Cartesian axis, $\delta(\cdot)$ is the delta distribution, and $f(\cdot)$ is a function of time. The expression of $f(\cdot)$ can be selected among different waveforms. Here, we report one of the most employed one, i.e. the Ricker wavelet [57], defined as

$$f(t) = A_0(1 - 2\beta_p(t - t_0)^2)e^{-\beta_p(t-t_0)^2}, \quad \beta_p = \pi^2 f_p^2, \quad (12)$$

being A_0 is the wave amplitude, f_p the peak frequency of the signal and t_0 is a fixed reference time.

To define a vertically incident plane wave one can consider a uniform distribution of body forces along the plane $z = z_0$ of the form $\mathbf{f}(\mathbf{x}, t) = f(t)\mathbf{e}_i\delta(z - z_0)$. The latter generates a displacement in the i^{th} direction of the form

$$\bar{u}_i(\mathbf{x}, t) = \frac{1}{2\rho c} H\left(t - \frac{|z - z_0|}{c}\right) \int_0^{t - \frac{|z - z_0|}{c}} f(\tau) d\tau, \quad (13)$$

where $H(\cdot)$ is the Heaviside function and c (that can be equal to $c_P = \sqrt{\lambda + 2\mu/\rho}$ or $c_S = \sqrt{\mu/\rho}$) is the wave velocity, see [58]. By taking the derivative with respect to time of (13) and evaluating the result at $z = z_0$ we can express $f(t)$ as $f(t) = 2\rho c \frac{\partial \bar{u}_i}{\partial t}$. Finally, we introduce one of the most important seismic input for seismic wave propagation that is the double-couple source force. A point double-couple or moment-tensor source localized in the computational domain is often adopted to simulate small local or near-regional earthquakes. Its mathematical representation is based on the seismic moment tensor $\mathbf{m}(\mathbf{x}, t)$, defined in [59] as

$$m_{ij}(\mathbf{x}, t) = \frac{M_0(\mathbf{x}, t)}{V} (s_{F,i}n_{F,j} + s_{F,j}n_{F,i}) \quad i, j = 1, \dots, d,$$

where \mathbf{n}_F and \mathbf{s}_F denote the fault normal and the rake vector along the fault, respectively. $M_0(\mathbf{x}, t)$ describes the time history of the moment release at \mathbf{x} and V is the force elementary volume. The equivalent body force distribution is finally obtained through the relation $\mathbf{f}(\mathbf{x}, t) = -\nabla \cdot \mathbf{m}(\mathbf{x}, t)$, see [60].

3 Discrete setting for PolyDG methods

3.1 Space discretization

In this section we define the notation related to the subdivision of the computational domain Ω by means of polytopic meshes. We introduce a polytopic mesh \mathcal{T}_h made of general polygons (in 2d) or polyhedra (in 3d). We denote such polytopic elements by κ , define by $|\kappa|$ their measure and by h_κ their diameter, and set $h = \max_{\kappa \in \mathcal{T}_h} h_\kappa$. We let a polynomial degree $p_\kappa \geq 1$ be associated with each element $\kappa \in \mathcal{T}_h$ and we denote by $p_h : \mathcal{T}_h \rightarrow \mathbb{N}^* = \{n \in \mathbb{N} \mid n \geq 1\}$ the piecewise constant function such that $(p_h)|_\kappa = p_\kappa$. The discrete spaces are introduced as follows: $\mathbf{V}_h = [\mathcal{P}_{p_h}(\mathcal{T}_h)]^d$, where $\mathcal{P}_{p_h}(\mathcal{T}_h)$ is the space of piecewise polynomials in Ω of total degree less than or equal to p_κ in any $\kappa \in \mathcal{T}_h$.

In order to deal with polygonal and polyhedral elements, we define an *interface* as the intersection of the $(d-1)$ -dimensional faces of any two neighboring elements of \mathcal{T}_h . If $d = 2$, an interface/face is a line segment and the set of all interfaces/faces is denoted by \mathcal{F}_h . When $d = 3$, an interface can be a general polygon that we assume could be further decomposed into a set of planar triangles collected in the set \mathcal{F}_h . We decompose the faces of \mathcal{T}_h into the union of *internal* (i) and *boundary* (b) faces, respectively, i.e.: $\mathcal{F}_h = \mathcal{F}_h^i \cup \mathcal{F}_h^b$. Moreover we further split the boundary faces as $\mathcal{F}_h^b = \mathcal{F}_h^D \cup \mathcal{F}_h^N$, meaning that on \mathcal{F}_h^D (resp. \mathcal{F}_h^N) Dirichlet (resp. Neumann) boundary conditions are applied.

Following [61], we next introduce the main assumption on \mathcal{T}_h .

Definition 3.1. *A mesh \mathcal{T}_h is said to be polytopic-regular if for any $\kappa \in \mathcal{T}_h$, there exists a set of non-overlapping d -dimensional simplices contained in κ , denoted by $\{S_\kappa^F\}_{F \subset \partial\kappa}$, such that for any $F \subset \partial\kappa$, the following condition holds:*

$$h_\kappa \lesssim d |S_\kappa^F| |F|^{-1}. \quad (14)$$

Assumption 3.1. *The sequence of meshes $\{\mathcal{T}_h\}_h$ is assumed to be uniformly polytopic regular in the sense of Definition 3.1.*

As pointed out in [61], this assumption does not impose any restriction on either the number of faces per element nor their measure relative to the diameter of the element they belong to. Under Assumption 3.1, the following *trace-inverse inequality* holds:

$$\|v\|_{L^2(\partial\kappa)} \lesssim p h_\kappa^{-1/2} \|v\|_{L^2(\kappa)} \quad \forall \kappa \in \mathcal{T}_h \quad \forall v \in \mathcal{P}_p(\kappa). \quad (15)$$

In order to avoid technicalities, we also make the following *hp-local bounded variation property* assumption.

Assumption 3.2. *For any pair of neighboring elements $\kappa^\pm \in \mathcal{T}_h$, it holds $h_{\kappa^+} \lesssim h_{\kappa^-} \lesssim h_{\kappa^+}$ and $p_{\kappa^+} \lesssim p_{\kappa^-} \lesssim p_{\kappa^+}$.*

Next, following [62], for sufficiently piecewise smooth scalar-, vector- and tensor-valued fields ψ , \mathbf{v} and $\boldsymbol{\tau}$, respectively, we define the averages and jumps on each *interior* face $F \in \mathcal{F}_h^i$ shared by the elements $\kappa^\pm \in \mathcal{T}_h$ as follows:

$$\begin{aligned} \llbracket \psi \rrbracket &= \psi^+ \mathbf{n}^+ + \psi^- \mathbf{n}^-, & \llbracket \mathbf{v} \rrbracket &= \mathbf{v}^+ \otimes \mathbf{n}^+ + \mathbf{v}^- \otimes \mathbf{n}^-, & \llbracket \mathbf{v} \rrbracket_{\mathbf{n}} &= \mathbf{v}^+ \cdot \mathbf{n}^+ + \mathbf{v}^- \cdot \mathbf{n}^-, \\ \{\psi\} &= \frac{\psi^+ + \psi^-}{2}, & \{\mathbf{v}\} &= \frac{\mathbf{v}^+ + \mathbf{v}^-}{2}, & \{\boldsymbol{\tau}\} &= \frac{\boldsymbol{\tau}^+ + \boldsymbol{\tau}^-}{2}, \end{aligned}$$

where \otimes is the tensor product in \mathbb{R}^3 , \cdot denotes the trace on F taken within κ^\pm , and \mathbf{n}^\pm is the outer normal vector to $\partial\kappa^\pm$. Accordingly, on *boundary* faces $F \in \mathcal{F}_h^b$, we set $\llbracket \psi \rrbracket = \psi \mathbf{n}$, $\{\psi\} = \psi$, $\llbracket \mathbf{v} \rrbracket = \mathbf{v} \otimes \mathbf{n}$, $\llbracket \mathbf{v} \rrbracket_{\mathbf{n}} = \mathbf{v} \cdot \mathbf{n}$, $\{\mathbf{v}\} = \mathbf{v}$, $\{\boldsymbol{\tau}\} = \boldsymbol{\tau}$.

Finally, we introduced some important concepts employed for the convergence analysis of PolyDG methods presented in the sequel, namely, the mesh covering $\mathcal{T}_\#$ and the Stein extension operator $\tilde{\mathcal{E}}$. Indeed, the latter are used to extend

standard hp -interpolation estimates on simplices to polytopal elements. We refer the reader to [36, 63, 40, 61] for all the details.

A covering $\mathcal{T}_{\sharp} = \{\mathcal{K}_{\kappa}\}$ related to the polytopic mesh \mathcal{T}_h is a set of shape regular d -dimensional simplices \mathcal{K}_{κ} such that for each $\kappa \in \mathcal{T}_h$ there exists a $\mathcal{K}_{\kappa} \in \mathcal{T}_{\sharp}$ such that $\kappa \subset \mathcal{K}_{\kappa}$. We suppose that there exists a covering \mathcal{T}_{\sharp} of \mathcal{T}_h and a positive constant C_{Ω} , independent of the mesh parameters, such that

$$\max_{\kappa \in \mathcal{T}_h} \text{card}\{\kappa' \in \mathcal{T}_h : \kappa' \cap \mathcal{K}_{\kappa} \neq \emptyset, \mathcal{K}_{\kappa} \in \mathcal{T}_{\sharp} \text{ s.t. } \kappa \subset \mathcal{K}_{\kappa}\} \leq C_{\Omega},$$

and $h_{T_{\kappa}} \lesssim h_{\kappa}$ for each pair $\kappa \in \mathcal{T}_{\kappa}$ and $T_{\kappa} \in \mathcal{T}_{\sharp}$ with $\kappa \subset T_{\kappa}$. This latter assumptions assure that, when the computational mesh \mathcal{T}_h is refined, the amount of overlap present in the covering \mathcal{T}_{\sharp} remains bounded.

For an open bounded domain $\Sigma \subset \mathbb{R}^d$ and a polytopic mesh \mathcal{T}_h over Σ satisfying Assumption 3.1, we can introduce the Stein extension operator $\tilde{\mathcal{E}} : H^m(\kappa) \rightarrow H^m(\mathbb{R}^d)$ [64], for any $\kappa \in \mathcal{T}_h$ and $m \in \mathbb{N}_0$, such that $\tilde{\mathcal{E}}v|_{\kappa} = v$ and $\|\tilde{\mathcal{E}}v\|_{m, \mathbb{R}^d} \lesssim \|v\|_{m, \kappa}$. The corresponding vector-valued version mapping $\mathbf{H}^m(\kappa)$ onto $\mathbf{H}^m(\mathbb{R}^d)$ acts component-wise and is denoted in the same way. In what follows, for any $\kappa \in \mathcal{T}_h$, we will denote by \mathcal{K}_{κ} the simplex belonging to \mathcal{T}_{\sharp} such that $\kappa \subset \mathcal{K}_{\kappa}$.

3.2 Time integration

We introduce here the time integration scheme used for the numerical simulations shown in the following sections. First, we observe that all the semi-discrete problems arising after a PolyDG discretization, i.e., equations (24), (36) and (54), can be rewritten in a compact form as $\mathbf{A}\ddot{X} + \mathbf{B}\dot{X} + \mathbf{C}X = \mathbf{F}$ or equivalently as

$$\ddot{X} = \mathbf{A}^{-1}(\mathbf{F} - \mathbf{B}\dot{X} - \mathbf{C}X) = \mathbf{A}^{-1}\mathbf{F} - \mathbf{A}^{-1}\mathbf{B}\dot{X} - \mathbf{A}^{-1}\mathbf{C}X = \mathcal{L}(t, X, \dot{X}). \quad (16)$$

Then, we discretize the interval $[0, T]$ by introducing a timestep $\Delta t > 0$, such that $\forall k \in \mathbb{N}$, $t_{k+1} - t_k = \Delta t$ and define X^k as $X^k = X(t^k)$, with X can be either U^T , $[U, W]^T$ or $[U, W, \Phi]^T$, depending on the problem we are solving. Finally, to integrate in time (16) we can apply the Newmark- β scheme as follows. The Newmark- β scheme is defined by introducing a Taylor expansion for displacement and velocity, respectively:

$$\begin{cases} X^{k+1} = X^k + \Delta t Z^k + \Delta t^2 (\beta_N \mathcal{L}^{k+1} + (\frac{1}{2} - \beta_N) \mathcal{L}^k), \\ Z^{k+1} = Z^k + \Delta t (\gamma_N \mathcal{L}^{k+1} + (1 - \gamma_N) \mathcal{L}^k), \end{cases} \quad (17)$$

being $Z^k = \dot{X}(t^k)$, $\mathcal{L}^k = \mathcal{L}(t^k, X^k, Z^k)$ and the Newmark parameters β_N and γ_N satisfy, the following constraints $0 \leq \gamma_N \leq 1$, $0 \leq 2\beta_N \leq 1$. The typical choices of parameters are $\gamma_N = 1/2$ and $\beta_N = 1/4$, for which the scheme is unconditionally stable and second order accurate. We also remark that when $\mathcal{L} = \mathcal{L}(t^k, X^k)$ $\beta = 0$ and $\gamma = 1/2$ the Newmark scheme reduces to the leap-frog scheme which is explicit and second order accurate.

4 Elastic wave propagation in heterogeneous media

Hereafter, for the sake of presentation, we will consider the linear visco elastodynamics model, i.e. equations (7) and (6). We suppose $\partial\Omega = \Gamma_D \cup \Gamma_N$ and we consider homogeneous Dirichlet and Neumann boundary conditions on Γ_D and Γ_N , respectively. The system of equations can be recast as

$$\begin{cases} \rho\partial_{tt}\mathbf{u} + 2\rho\zeta\partial_t\mathbf{u} + \rho\zeta^2\mathbf{u} - \nabla \cdot \boldsymbol{\sigma} = \mathbf{f} & \text{in } \Omega \times (0, T], \\ \boldsymbol{\sigma} = \mathbb{D}\boldsymbol{\epsilon}(\mathbf{u}) = \lambda\nabla \cdot \boldsymbol{\epsilon}(\mathbf{u})\mathbf{I} + 2\mu\boldsymbol{\epsilon}(\mathbf{u}), & \text{in } \Omega \times (0, T], \\ \mathbf{u} = \mathbf{0} & \text{on } \Gamma_D \times (0, T], \\ \boldsymbol{\sigma}\mathbf{n} = \mathbf{0} & \text{on } \Gamma_N \times (0, T], \\ (\mathbf{u}, \partial_t\mathbf{u}) = (\mathbf{u}_0, \mathbf{u}_1) & \text{in } \Omega \times \{0\}. \end{cases} \quad (18)$$

The case with non homogenous Neumann conditions is treated in [65], while absorbing conditions are considered in [54]. Finally, we refer to [18, 66] for a detailed analysis of viscoelastic attenuation models. We suppose the mass density ρ and the Lamé parameters λ and μ strictly positive bounded functions of the space variable \mathbf{x} , i.e. $\rho, \lambda, \mu \in L^\infty(\Omega)$. We also suppose the forcing term \mathbf{f} a given (regular enough) source terms, i.e., $\mathbf{f} \in L^2((0, T]; \mathbf{L}^2(\Omega))$ and that the initial conditions $(\mathbf{u}_0, \mathbf{u}_1) \in \mathbf{H}_0^1(\Omega) \times \mathbf{L}^2(\Omega)$. The weak formulation of problem (18) reads as follows: for all $t \in (0, T]$ find $\mathbf{u} = \mathbf{u}(t) \in \mathbf{H}_0^1(\Omega)$ such that

$$(\rho\partial_{tt}\mathbf{u}, \mathbf{v})_\Omega + (2\rho\zeta\partial_t\mathbf{u}, \mathbf{v})_\Omega + (\rho\zeta^2\mathbf{u}, \mathbf{v})_\Omega + \mathcal{A}^e(\mathbf{u}, \mathbf{v}) = (\mathbf{f}, \mathbf{v})_\Omega \quad \forall \mathbf{v} \in \mathbf{H}_0^1(\Omega), \quad (19)$$

where for any $\mathbf{u}, \mathbf{v} \in \mathbf{H}_0^1(\Omega)$ we have set

$$\mathcal{A}^e(\mathbf{u}, \mathbf{v}) = (\boldsymbol{\sigma}(\mathbf{u}), \boldsymbol{\epsilon}(\mathbf{v}))_\Omega. \quad (20)$$

Problem (19) is well-posed and its unique solution $\mathbf{u} \in C((0, T]; \mathbf{H}_0^1(\Omega)) \cap C^1((0, T]; \mathbf{L}^2(\Omega))$, see [67, Theorem 8-3.1].

4.1 Semi-discrete formulation

Using the notation introduced in Section 3, we define the PolyDG semi-discretization of problem (19): for all $t \in (0, T]$, find $\mathbf{u}_h = \mathbf{u}_h(t) \in \mathbf{V}_h$ such that

$$(\rho\partial_{tt}\mathbf{u}_h, \mathbf{v}_h)_\Omega + (2\rho\zeta\partial_t\mathbf{u}_h, \mathbf{v}_h)_\Omega + (\rho\zeta^2\mathbf{u}_h, \mathbf{v}_h)_\Omega + \mathcal{A}_h^e(\mathbf{u}_h, \mathbf{v}_h) = (\mathbf{f}, \mathbf{v}_h)_\Omega \quad (21)$$

for any $\mathbf{v}_h \in \mathbf{V}_h$, supplemented with the initial conditions $(\mathbf{u}_h(0), \partial_t\mathbf{u}_h(0)) = (\mathbf{u}_h^0, \mathbf{u}_h^1)$, where $\mathbf{u}_h^0, \mathbf{u}_h^1 \in \mathbf{V}_h$ are suitable approximations of \mathbf{u}_0 and \mathbf{u}_1 , respectively. Here, we also assume the stiffness tensor \mathbb{D} and the mass density ρ to be element-wise constant over \mathcal{T}_h . The bilinear form $\mathcal{A}_h^e : \mathbf{V}_h \times \mathbf{V}_h \rightarrow \mathbb{R}$ is defined as

$$\mathcal{A}_h^e(\mathbf{u}, \mathbf{v}) = (\boldsymbol{\sigma}(\mathbf{u}), \boldsymbol{\epsilon}(\mathbf{v}))_{\mathcal{T}_h} - (\{\boldsymbol{\sigma}(\mathbf{u})\}, \llbracket \mathbf{v} \rrbracket)_{\mathcal{F}_h^i \cup \mathcal{F}_h^D}$$

$$-([\mathbf{u}], \{\boldsymbol{\sigma}(\mathbf{v})\})_{\mathcal{F}_h^i \cup \mathcal{F}_h^D} + (\eta[\mathbf{u}], [\mathbf{v}])_{\mathcal{F}_h^i \cup \mathcal{F}_h^D} \quad (22)$$

for all $\mathbf{u}, \mathbf{v} \in \mathbf{V}_h$. Here, we adopt the compact notation $(\cdot, \cdot)_{\mathcal{T}_h} = \sum_{T \in \mathcal{T}_h} (\cdot, \cdot)_T$ and $(\cdot, \cdot)_{\mathcal{F}_h^i \cup \mathcal{F}_h^D} = \sum_{F \in \mathcal{F}_h^i \cup \mathcal{F}_h^D} (\cdot, \cdot)_F$. The penalization function $\eta : \mathcal{F}_h \rightarrow \mathbb{R}^+$ in (22) is defined face-wise as

$$\eta = \sigma_0 \begin{cases} \max_{\kappa \in \{\kappa_1, \kappa_2\}} (\overline{\mathbb{D}}_\kappa p_\kappa^2 h_\kappa^{-1}), & F \in \mathcal{F}_h^i, F \subset \partial\kappa_1 \cap \partial\kappa_2, \\ \overline{\mathbb{D}}_\kappa p_\kappa^2 h_\kappa^{-1}, & F \in \mathcal{F}_h^D, F \subset \partial\kappa \cap \Gamma_D. \end{cases} \quad (23)$$

where $\overline{\mathbb{D}}_\kappa = |\mathbb{D}(\cdot)_\kappa|^{1/2} \|\cdot\|_2^2$ for any $\kappa \in \mathcal{T}_h$ (here $\|\cdot\|_2$ is the operator norm induced by the l_2 -norm on \mathbb{R}^n , where n denotes the dimension of the space of symmetric second-order tensors, i.e., $n = 3$ if $d = 2$, $n = 6$ if $d = 3$), and σ_0 is a (large enough) positive parameter at our disposal.

By fixing a basis for \mathbf{V}_h and denoting by \mathbf{U} the vector of the expansion coefficients in the chosen basis of the unknown \mathbf{u}_h the semi-discrete formulation (21) can be written equivalently as:

$$\mathbf{M}_\rho \ddot{\mathbf{U}}(t) + \mathbf{D} \dot{\mathbf{U}}(t) + (\mathbf{A}^e + \mathbf{C}) \mathbf{U}(t) = \mathbf{F}(t) \quad \forall t \in (0, T), \quad (24)$$

with \mathbf{M} denoting the mass matrix in \mathbf{V}_h , \mathbf{A}^e the stiffness matrix corresponding to the bilinear form \mathcal{A}^e , \mathbf{D} and \mathbf{C} the damping matrices, and with initial conditions $\mathbf{U}(0) = \mathbf{U}_0$ and $\dot{\mathbf{U}}(0) = \mathbf{U}_1$. Note that \mathbf{F} is the vector representations of the linear functional $(\mathbf{f}, \mathbf{v}_h)_\Omega$.

4.2 Stability and convergence results

In this section we recall the stability and convergence results for the semidiscrete PolyDG formulation (21). We refer the reader to [45] and to [68] for all the details. The results are obtained in the following energy norm

$$\|\mathbf{u}_h(t)\|_{\mathbb{E}}^2 = \|\rho^{\frac{1}{2}} \partial_t \mathbf{u}_h(t)\|_{\Omega}^2 + \|\rho^{\frac{1}{2}} \zeta \mathbf{u}_h(t)\|_{\Omega}^2 + \|\mathbf{u}_h(t)\|_{\text{DG},e}^2 \quad \forall t \in (0, T], \quad (25)$$

where

$$\|\mathbf{v}\|_{\text{DG},e}^2 = \|\mathbb{D}^{\frac{1}{2}} \boldsymbol{\epsilon}(\mathbf{v})\|_{\mathcal{T}_h}^2 + \|\eta^{\frac{1}{2}} [\mathbf{v}]\|_{\mathcal{F}_h^i \cup \mathcal{F}_h^D}^2 \quad \forall \mathbf{v} \in \mathbf{V}_h \oplus \mathbf{H}_0^1(\Omega), \quad (26)$$

with $\|\cdot\|_{\mathcal{T}_h}^2 = (\cdot, \cdot)_{\mathcal{T}_h}$ and $\|\cdot\|_{\mathcal{F}_h^i \cup \mathcal{F}_h^D}^2 = (\cdot, \cdot)_{\mathcal{F}_h^i \cup \mathcal{F}_h^D}$.

Proposition 4.1. *Let $\mathbf{f} \in L^2((0, T]; \mathbf{L}^2(\Omega))$ and $\mathbf{u}_h \in C^1((0, T]; \mathbf{V}_h)$ be the approximate solution of (21) obtained with the stability constant σ_0 defined in (23) chosen sufficiently large. Then,*

$$\|\mathbf{u}_h(t)\|_{\mathbb{E}} \lesssim \|\mathbf{u}_h^0\|_{\mathbb{E}} + \int_0^t \|\mathbf{f}(\tau)\|_{\mathbf{L}^2(\Omega)} d\tau, \quad \forall 0 < t \leq T, \quad (27)$$

where $\|\mathbf{u}_h(0)\|_E^2 = \|\rho^{\frac{1}{2}}\mathbf{u}_{1,h}\|_\Omega^2 + \|\rho^{\frac{1}{2}}\zeta\mathbf{u}_{0,h}\|_\Omega^2 + \|\mathbf{u}_{0,h}\|_{\text{DG},e}^2$, being $\mathbf{u}_{0,h}, \mathbf{u}_{1,h} \in \mathbf{V}_h$ suitable approximation of the initial conditions \mathbf{u}_0 and \mathbf{u}_1 , respectively. The proof of the previous stability estimate can be found for instance in [45, 68]. From (27) it is possible to conclude that the PolyDG approximation is dissipative. Indeed, when $\mathbf{f} = \mathbf{0}$ (no external forces) the energy of the system at rest $\|\mathbf{u}_h^0\|_E$ is not conserved through time.

Concerning the convergence results of the PolyDG scheme we report here below the main result. We refer the reader to [45] for the details and for the proof of the following theorem.

Theorem 4.1. *Let Assumption 3.1 and Assumption 3.2 be satisfied and assume that the exact solution \mathbf{u} of (19) is sufficiently regular. For any time $t \in [0, T]$, let $\mathbf{u}_h \in \mathbf{V}_h$ be the PolyDG solution of problem (21) obtained with a penalty parameter σ_0 appearing in (23) sufficiently large. Then, for any time $t \in (0, T]$ the following bound holds*

$$\|\mathbf{u} - \mathbf{u}_h\|_E(t) \lesssim \sum_{\kappa \in \mathcal{T}_h} \frac{h_\kappa^{s_\kappa - 1}}{p_\kappa^{m_\kappa - 3/2}} \left(\mathcal{I}_{m_\kappa}^{\mathcal{T}_\sharp}(\mathbf{u})(t) + \int_0^t \mathcal{I}_{m_\kappa}^{\mathcal{T}_\sharp}(\partial_t \mathbf{u})(s) ds \right), \quad (28)$$

where

$$\mathcal{I}_{m_\kappa}^{\mathcal{T}_\sharp}(\mathbf{u}) = \|\tilde{\mathcal{E}}\mathbf{u}\|_{\mathbf{H}^{m_\kappa}(\mathcal{T}_\sharp)} + \frac{h_\kappa}{3/2} \|\tilde{\mathcal{E}}(\partial_t \mathbf{u})\|_{\mathbf{H}^{m_\kappa}(\mathcal{T}_\sharp)} + \|\tilde{\mathcal{E}}\boldsymbol{\sigma}(\mathbf{u})\|_{\mathbf{H}^{m_\kappa}(\mathcal{T}_\sharp)}$$

with $s_\kappa = \min(p_\kappa + 1, m_\kappa)$ for all $\kappa \in \mathcal{T}_h$. The hidden constant depends on the material parameters and the shape-regularity of the covering \mathcal{T}_\sharp , but is independent of h_κ, p_κ .

4.3 Verification test

We solve the wave propagation problem (18) in $\Omega = (0, 1)^2$, choosing $\lambda = \mu = \rho = \zeta = 1$ and assuming that the analytical solution \mathbf{u} is given by

$$\mathbf{u}(\mathbf{x}, t) = \sin(\sqrt{2}\pi t) \begin{bmatrix} -\sin(\pi x)^2 \sin(2\pi y) \\ \sin(2\pi x) \sin(\pi y)^2 \end{bmatrix}. \quad (29)$$

Dirichlet boundary conditions and initial conditions are set accordingly. We set the final time $T = 1$ and chose a time step $\Delta t = 10^{-4}$ of the leap-frog scheme, cf. (17). The penalty parameter σ_0 appearing in (23) has been set equal to 10. We compute the discretization error by varying the polynomial degree $p_\kappa = p$, for any $\kappa \in \mathcal{T}_h$, and the number of polygonal elements N_{el} .

In Figure 3 (left), we report the computed \mathbf{L}^2 -error $\|e_{\mathbf{u}}\|_{\mathbf{L}^2(\Omega)} = \|\mathbf{u} - \mathbf{u}_h\|_{\mathbf{L}^2(\Omega)}$ at time T obtained on a shape-regular polygonal grid (cf. Figure 2) versus the polynomial degree p , which varies from 1 to 5, in semilogarithmic scale. We fix the number of polygonal elements as $N_{el} = 160$. We observe the exponential converge in p , since the chosen solution is analytic. Next, we compute the energy error $\|\mathbf{u} - \mathbf{u}_h\|_E$ at final time T as a function of the mesh size h , as shown in Figure 3 (right). In this case we retrieve the algebraic convergence proved in (28) for a polynomial degree $p = 2, 3, 4$.

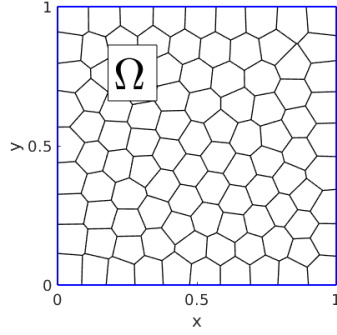


Fig. 2: Test case of Section 4.3. Example of computational domain having 100 polygonal elements.

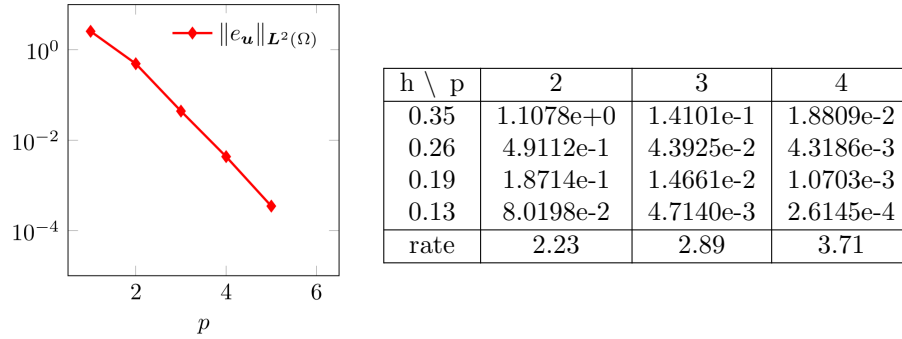


Fig. 3: Test case of Section 4.3. (Left) Computed L^2 -error as a function of the polynomial degree p in a semilogarithmic scale by fixing the number of polygonal elements as $N_{el} = 160$. (Right) Computed energy error as a function of the mesh size h for polynomial degree $p = 2, 3, 4$. The rate of convergence is also reported in the last row, cf. (28).

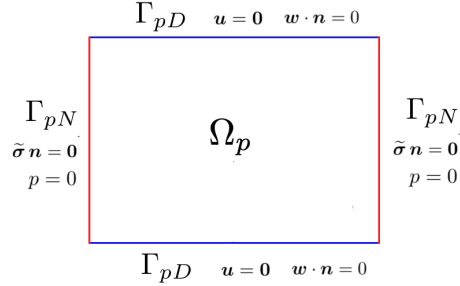


Fig. 4: Example of porous domain Ω_p together with mixed boundary conditions on Γ_{pD} and Γ_{pN} .

5 Poro-elastic media

In this section, we consider a poro-elastic material occupying a polyhedral domain $\Omega_p \subset \Omega$ modeled by equations (9) and (10). The low-frequency Biot's system [20] can be written as

$$\begin{cases}
 \rho \partial_{tt} \mathbf{u} + \rho_f \partial_{tt} \mathbf{w} - \nabla \cdot \tilde{\boldsymbol{\sigma}} = \mathbf{f} & \text{in } \Omega_p \times (0, T], \\
 \tilde{\boldsymbol{\sigma}} = \lambda \nabla \cdot \boldsymbol{\epsilon}(\mathbf{u}) \mathbf{I} + 2\mu \boldsymbol{\epsilon}(\mathbf{u}) - \beta p \mathbf{I} & \text{in } \Omega_p \times (0, T], \\
 \rho_f \partial_{tt} \mathbf{u} + \rho_w \partial_{tt} \mathbf{w} + \frac{\eta}{k} \dot{\mathbf{w}} + \nabla p = \mathbf{g} & \text{in } \Omega_p \times (0, T], \\
 p = -m(\beta \nabla \cdot \mathbf{u} + \nabla \cdot \mathbf{w}) & \text{in } \Omega_p \times (0, T], \\
 \mathbf{u} = \mathbf{0} \quad \text{and} \quad \mathbf{w} \cdot \mathbf{n} = 0 & \text{on } \Gamma_{pD} \times (0, T], \\
 \tilde{\boldsymbol{\sigma}} \mathbf{n} = \mathbf{0} \quad \text{and} \quad p = 0 & \text{on } \Gamma_{pN} \times (0, T], \\
 (\mathbf{u}, \partial_t \mathbf{u}) = (\mathbf{u}_0, \mathbf{u}_1) & \text{in } \Omega_p \times \{0\}, \\
 (\mathbf{w}, \partial_t \mathbf{w}) = (\mathbf{w}_0, \mathbf{w}_1) & \text{in } \Omega_p \times \{0\},
 \end{cases} \quad (30)$$

where the density ρ_w is given by $\rho_w = a\phi^{-1}\rho_f$ with tortuosity $a > 1$, η represents the dynamic viscosity of the fluid, k is the absolute permeability, and m denotes the Biot modulus. As in the previous section, we assume that the model coefficients $\rho_f, \rho_w, \eta k^{-1}, m \in L^\infty(\Omega_p)$ are strictly positive scalar fields and that the source term \mathbf{f}, \mathbf{g} and the initial conditions $(\mathbf{w}_0, \mathbf{w}_1)$ are regular vector fields, namely $\mathbf{f}, \mathbf{g} \in L^2((0, T]; \mathbf{L}^2(\Omega_p))$ and $(\mathbf{w}_0, \mathbf{w}_1) \in \mathbf{H}_0(\text{div}, \Omega_p) \times \mathbf{L}^2(\Omega_p)$. The third and fourth equations in (30) correspond to the dynamic Darcy's law and the conservation of fluid mass, respectively. For the sake of simplicity, in (30) we have also assumed that the clamped region $\Gamma_{pD} \subset \partial\Omega_p$ is impermeable and a null pore pressure condition is prescribed on the Neumann boundary $\Gamma_{pN} = \partial\Omega_p \setminus \Gamma_{pD}$, cf. Figure 4. We remark that more general boundary conditions can be treated up to minor modifications.

In what follows, we focus on the two-displacement formulation of the low frequency poro-elasticity problem [69], that is obtained by inserting the expression of the total stress $\tilde{\boldsymbol{\sigma}}$ and the pore pressure p in the other equations in (30). The corresponding weak formulation reads: for all $t \in (0, T]$ find

$(\mathbf{u}(t), \mathbf{w}(t)) \in \mathbf{H}_0^1(\Omega_p) \times \mathbf{H}_0(\text{div}, \Omega_p)$ such that

$$\begin{aligned} & \mathcal{M}^P((\partial_{tt}\mathbf{u}, \partial_{tt}\mathbf{w}), (\mathbf{v}, \mathbf{z})) + (\eta k^{-1} \partial_t \mathbf{w}, \mathbf{z})_{\Omega_p} + \mathcal{A}^e(\mathbf{u}, \mathbf{v}) + \mathcal{A}^P(\beta \mathbf{u} + \mathbf{w}, \beta \mathbf{v} + \mathbf{z}) \\ & = (\mathbf{f}, \mathbf{v})_{\Omega_p} + (\mathbf{g}, \mathbf{z})_{\Omega_p}, \quad \forall (\mathbf{v}, \mathbf{z}) \in \mathbf{H}_0^1(\Omega_p) \times \mathbf{H}_0(\text{div}, \Omega_p), \end{aligned} \quad (31)$$

with $\mathcal{A}^e : \mathbf{H}_0^1(\Omega_p) \times \mathbf{H}_0^1(\Omega_p) \rightarrow \mathbb{R}$ defined as the restriction to Ω_p of in (20) and the bilinear forms $\mathcal{M}^P, \mathcal{A}^P$ defined such that

$$\begin{aligned} \mathcal{M}^P((\mathbf{u}, \mathbf{w}), (\mathbf{v}, \mathbf{z})) & = (\rho \mathbf{u} + \rho_f \mathbf{w}, \mathbf{v})_{\Omega_p} + (\rho_f \mathbf{u} + \rho_w \mathbf{w}, \mathbf{z})_{\Omega_p}, \\ \mathcal{A}^P(\mathbf{w}, \mathbf{z}) & = (m \nabla \cdot \mathbf{w}, \nabla \cdot \mathbf{z})_{\Omega_p}, \end{aligned} \quad (32)$$

for all $(\mathbf{u}, \mathbf{w}), (\mathbf{v}, \mathbf{z}) \in \mathbf{H}_0^1(\Omega_p) \times \mathbf{H}_0(\text{div}, \Omega_p)$. The well-posedness of the low-frequency poro-elasticity problem (31) has been established in [70, Section 5.2] in the framework of semigroup theory.

5.1 Semi-discrete formulation

Proceeding as in Section 4.1, we derive the semi-discrete PolydG approximation of problem (31). We introduce a polytopic mesh \mathcal{T}_h^p of Ω_p satisfying Assumptions 3.1 and 3.2 and denote by \mathcal{F}_h^p the set of faces of \mathcal{T}_h^p . Here, we consider the same polynomial space for both the discrete solid displacement \mathbf{u}_h and filtration displacement \mathbf{w}_h , i.e. $\mathbf{u}_h, \mathbf{w}_h \in \mathbf{V}_h^p = (\mathcal{P}_{p_h}(\mathcal{T}_h^p))^d$, and we assume that all the model coefficients are piecewise constant over \mathcal{T}_h^p . The PolydG semi-discrete problem consists in finding, for all $t \in (0, T]$, the solution $(\mathbf{u}_h(t), \mathbf{w}_h(t)) \in \mathbf{V}_h^p \times \mathbf{V}_h^p$ such that

$$\begin{aligned} & \mathcal{M}^P((\partial_{tt}\mathbf{u}_h, \partial_{tt}\mathbf{w}_h), (\mathbf{v}_h, \mathbf{z}_h)) + (\eta k^{-1} \partial_t \mathbf{w}_h, \mathbf{z}_h)_{\Omega_p} + \mathcal{A}_h^e(\mathbf{u}_h, \mathbf{v}_h) \\ & + \mathcal{A}_h^P(\beta \mathbf{u}_h + \mathbf{w}_h, \beta \mathbf{v}_h + \mathbf{z}_h) = (\mathbf{f}, \mathbf{v}_h)_{\Omega_p} + (\mathbf{g}, \mathbf{z}_h)_{\Omega_p}, \quad \forall \mathbf{v}_h, \mathbf{z}_h \in \mathbf{V}_h^p, \end{aligned} \quad (33)$$

where $\mathcal{A}_h^e : \mathbf{V}_h^p \times \mathbf{V}_h^p \rightarrow \mathbb{R}$ is defined as in (22) and the bilinear form \mathcal{A}_h^P defined such that

$$\begin{aligned} \mathcal{A}_h^P(\mathbf{w}, \mathbf{z}) & = (m \nabla \cdot \mathbf{w}, \nabla \cdot \mathbf{z})_{\mathcal{T}_h^p} - (\{m(\nabla \cdot \mathbf{w})\}, \llbracket \mathbf{z} \rrbracket_{\mathbf{n}})_{\mathcal{F}_h^{p,i} \cup \mathcal{F}_h^{p,D}} \\ & - (\llbracket \mathbf{w} \rrbracket_{\mathbf{n}}, \{m(\nabla \cdot \mathbf{z})\})_{\mathcal{F}_h^{p,i} \cup \mathcal{F}_h^{p,D}} + (\gamma \llbracket \mathbf{w} \rrbracket_{\mathbf{n}}, \llbracket \mathbf{z} \rrbracket_{\mathbf{n}})_{\mathcal{F}_h^{p,i} \cup \mathcal{F}_h^{p,D}}, \end{aligned} \quad (34)$$

for all $\mathbf{w}, \mathbf{z} \in \mathbf{V}_h^p$ and the penalization function $\gamma \in L^\infty(\mathcal{F}_h^p)$ is given by

$$\gamma = m_0 \begin{cases} \max_{\kappa \in \{\kappa_1, \kappa_2\}} (m_{|\kappa} p_\kappa^2 h_\kappa^{-1}), & F \in \mathcal{F}_h^{p,i}, F \subset \partial \kappa_1 \cap \partial \kappa_2, \\ m_{|\kappa} p_\kappa^2 h_\kappa^{-1}, & F \in \mathcal{F}_h^{p,D}, F \subset \partial \kappa \cap \Gamma_{p,D}, \end{cases} \quad (35)$$

where m_0 is a positive user-dependent parameter. We remark that, owing to the $\mathbf{H}(\text{div})$ -regularity of the filtration displacement \mathbf{w} solving (31), the penalization term in (34) acts only on the normal component of the jumps. Problem (33) is completed with suitable initial conditions $(\mathbf{u}_h(0), \mathbf{w}_h(0), \partial_t \mathbf{u}_h(0), \partial_t \mathbf{w}_h(0)) = (\mathbf{u}_h^0, \mathbf{w}_h^0, \mathbf{u}_h^1, \mathbf{w}_h^1) \in \mathbf{V}_h^p \times \mathbf{V}_h^p \times \mathbf{V}_h^p \times \mathbf{V}_h^p$.

We conclude this section by observing that the algebraic representation of the semi-discrete formulation (33) is given by

$$\begin{bmatrix} \mathbf{M}_{\rho}^p & \mathbf{M}_{\rho_f}^p \\ \mathbf{M}_{\rho_f}^p & \mathbf{M}_{\rho_w}^p \end{bmatrix} \begin{bmatrix} \dot{U} \\ \dot{W} \end{bmatrix} + \begin{bmatrix} 0 & 0 \\ 0 & \mathbf{M}_{\eta k^{-1}} \end{bmatrix} \begin{bmatrix} \dot{U} \\ \dot{W} \end{bmatrix} + \begin{bmatrix} \mathbf{A}^e + \mathbf{A}_{\beta^2}^p & \mathbf{A}_{\beta}^p \\ \mathbf{A}_{\beta}^p & \mathbf{A}^p \end{bmatrix} \begin{bmatrix} U \\ W \end{bmatrix} = \begin{bmatrix} \mathbf{F} \\ \mathbf{G} \end{bmatrix}, \quad (36)$$

with initial conditions $[U, W, \dot{U}, \dot{W}](0) = [U_0, W_0, U_1, W_1]$ and $[\mathbf{F}, \mathbf{G}]^T$ corresponding to the vector representations of the linear functionals in the right-hand side of (33).

5.2 Stability and convergence results

The aim of this section is to establish an a priori estimate for the solution of problem (33). First, we define for all $\mathbf{u}, \mathbf{w} \in C^1([0, T]; \mathbf{V}_h^p)$ the energy function

$$\begin{aligned} \|(\mathbf{u}, \mathbf{w})(t)\|_{\mathcal{E}}^2 &= \|\rho_u^{\frac{1}{2}} \partial_t \mathbf{u}(t)\|_{\Omega_p}^2 + \|(\rho_f \phi)^{\frac{1}{2}} \partial_t (\mathbf{u} + \phi^{-1} \mathbf{w})(t)\|_{\Omega_p}^2 + \|\mathbf{u}(t)\|_{\text{DG}, e}^2 \\ &+ \|(\beta \mathbf{u} + \mathbf{w})(t)\|_{\text{DG}, p}^2 + \|(\eta/k)^{\frac{1}{2}} \mathbf{w}(0)\|_{\Omega_p}^2 + \int_0^t \|(\eta/k)^{\frac{1}{2}} \partial_t \mathbf{w}(s)\|_{\Omega_p}^2 ds, \end{aligned} \quad (37)$$

with $\rho_u = \frac{\rho_s(1-\phi)}{2}$, the norm $\|\cdot\|_{\text{DG}, e} : \mathbf{V}_h^p \rightarrow \mathbb{R}^+$ defined as in (26) and

$$\|\mathbf{z}\|_{\text{DG}, p}^2 = \|\mathbf{m}^{\frac{1}{2}} \nabla \cdot \mathbf{z}\|_{\mathcal{T}_h^p}^2 + \|\gamma^{\frac{1}{2}} \llbracket \mathbf{z} \rrbracket_{\mathbf{n}}\|_{\mathcal{F}_h^p \cup \mathcal{F}_h^D}^2 \quad \forall \mathbf{z} \in \mathbf{V}_h^p \oplus \mathbf{H}_0(\text{div}, \Omega_p). \quad (38)$$

One can easily check that $\max_{0 \leq t \leq T} \|(\cdot, \cdot)(t)\|_{\mathcal{E}}^2$ defines a norm on $C^1([0, T]; \mathbf{V}_h^p \times \mathbf{V}_h^p)$, cf. [49, Remark 3.2]. We are now ready to derive the stability estimate for the PolydG semi-discretization.

Proposition 5.1. *Let $\mathbf{f}, \mathbf{g} \in L^2((0, T]; \mathbf{L}^2(\Omega_p))$ and let $\mathbf{u}_h, \mathbf{w}_h \in C^1((0, T]; \mathbf{V}_h^p)$ be the solutions of (33) obtained with sufficiently large penalization parameters σ_0 and m_0 . Let additionally assume that $\rho_u^{-1}, k\eta^{-1} \in L^\infty(\Omega_p)$. Then, it holds*

$$\max_{t \in [0, T]} \|(\mathbf{u}_h, \mathbf{w}_h)(t)\|_{\mathcal{E}} \leq \int_0^T \left\| (k/\eta)^{\frac{1}{2}} \mathbf{g}(s) \right\|_{\Omega_p}^2 ds + T \int_0^T \left\| \rho_u^{-\frac{1}{2}} \mathbf{f}(s) \right\|_{\Omega_p}^2 ds + \mathcal{E}_0,$$

with

$$\begin{aligned} \mathcal{E}_0 &= \mathcal{E}_0(\mathbf{u}_h^0, \mathbf{w}_h^0, \mathbf{u}_h^1, \mathbf{w}_h^1) = \mathcal{M}^p((\mathbf{u}_h^1, \mathbf{w}_h^1), (\mathbf{u}_h^1, \mathbf{w}_h^1)) + \mathcal{A}_h^e(\mathbf{u}_h^0, \mathbf{u}_h^0) \\ &+ \mathcal{A}_h^p(\beta \mathbf{u}_h^0 + \mathbf{w}_h^0, \beta \mathbf{u}_h^0 + \mathbf{w}_h^0) + \|(\eta/k)^{\frac{1}{2}} \mathbf{w}_h^0\|_{\Omega_p}^2. \end{aligned} \quad (39)$$

Proof. First, we observe that the bilinear form \mathcal{M}^p is positive definite. Indeed, owing to the definition of the density functions ρ, ρ_u , and ρ_w and since $\tilde{a} = a - 1 > 0$, for all $(\mathbf{v}, \mathbf{z}) \neq (\mathbf{0}, \mathbf{0})$ one has

$$\begin{aligned} \mathcal{M}^p((\mathbf{v}, \mathbf{z}), (\mathbf{v}, \mathbf{z})) &= 2 \left\| \rho_u^{\frac{1}{2}} \mathbf{v} \right\|_{\Omega_p}^2 + \left\| (\rho_f \phi)^{\frac{1}{2}} \left(\mathbf{v} + \frac{\mathbf{z}}{\phi} \right) \right\|_{\Omega_p}^2 + \left\| \frac{(\rho_f \tilde{a})^{\frac{1}{2}} \mathbf{z}}{\phi^{\frac{1}{2}}} \right\|_{\Omega_p}^2 \\ &> 2 \left\| \rho_u^{\frac{1}{2}} \mathbf{v} \right\|_{\Omega_p}^2 + \left\| (\rho_f \phi)^{\frac{1}{2}} (\mathbf{v} + \phi^{-1} \mathbf{z}) \right\|_{\Omega_p}^2 > 0. \end{aligned} \quad (40)$$

Furthermore, if the stability parameters σ_0 and m_0 are chosen sufficiently large, the bilinear forms \mathcal{A}_h^e and \mathcal{A}_h^p are coercive (see [49, Lemma A.3]), i.e., for all $\mathbf{v}_h, \mathbf{z}_h \in \mathbf{V}_h^p$ it holds

$$\begin{aligned} \mathcal{A}_h^e(\mathbf{v}_h, \mathbf{v}_h) &\geq \|\mathbf{v}_h\|_{\text{DG},e}^2, \\ \mathcal{A}_h^p(\beta\mathbf{v}_h + \mathbf{z}_h, \beta\mathbf{v}_h + \mathbf{z}_h) &\geq |\beta\mathbf{v}_h + \mathbf{z}_h|_{\text{DG},p}^2. \end{aligned} \quad (41)$$

Then, taking $(\mathbf{v}_h, \mathbf{z}_h) = (\partial_t \mathbf{u}_h, \partial_t \mathbf{w}_h)$ in (33) and integrating in time between 0 and $t \leq T$, it is inferred that

$$\begin{aligned} &[\mathcal{M}^p((\partial_t \mathbf{u}_h, \partial_t \mathbf{w}_h), (\partial_t \mathbf{u}_h, \partial_t \mathbf{w}_h)) + \mathcal{A}_h^e(\mathbf{u}_h, \mathbf{u}_h) + \mathcal{A}_h^p(\beta\mathbf{u}_h + \mathbf{w}_h, \beta\mathbf{u}_h + \mathbf{w}_h)](t) \\ &+ 2 \int_0^t \left\| \left(\frac{\eta}{k} \right)^{\frac{1}{2}} \partial_t \mathbf{w}_h(s) \right\|_{\Omega_p}^2 ds = 2 \int_0^t (\mathbf{f}, \partial_t \mathbf{u}_h)_{\Omega_p}(s) + (\mathbf{g}, \partial_t \mathbf{w}_h)_{\Omega_p}(s) ds + \tilde{\mathcal{E}}_0, \end{aligned}$$

with $\tilde{\mathcal{E}}_0 = \mathcal{M}^p((\mathbf{u}_h^1, \mathbf{w}_h^1), (\mathbf{u}_h^1, \mathbf{w}_h^1)) + \mathcal{A}_h^e(\mathbf{u}_h^0, \mathbf{u}_h^0) + \mathcal{A}_h^p(\beta\mathbf{u}_h^0 + \mathbf{w}_h^0, \beta\mathbf{u}_h^0 + \mathbf{w}_h^0)$. Now, using (40) and (41) to infer a lower bound for the left-hand side of the previous identity and summing $\|(\eta/k)^{\frac{1}{2}} \mathbf{w}_h^0\|_{\Omega_p}^2$ to both sides of the resulting inequality, we obtain

$$\begin{aligned} \|\mathbf{u}_h, \mathbf{w}_h(t)\|_{\mathcal{E}} + \left\| \rho_u^{\frac{1}{2}} \partial_t \mathbf{u}_h(t) \right\|_{\Omega_p}^2 + \int_0^t \left\| (\eta/k)^{\frac{1}{2}} \partial_t \mathbf{w}_h(s) \right\|_{\Omega_p}^2 ds \\ \leq 2 \int_0^t (\mathbf{f}, \partial_t \mathbf{u}_h)_{\Omega_p}(s) + (\mathbf{g}, \partial_t \mathbf{w}_h)_{\Omega_p}(s) ds + \mathcal{E}_0, \end{aligned} \quad (42)$$

where $\mathcal{E}_0 = \tilde{\mathcal{E}}_0 + \|(\eta/k)^{\frac{1}{2}} \mathbf{w}_h^0\|_{\Omega_p}^2$ corresponds to the quantity defined in (39). Therefore, to conclude it only remains to bound the right-hand side of (42). To do so, we apply the Cauchy–Schwarz and Young inequalities to infer

$$2 \int_0^t (\mathbf{g}, \partial_t \mathbf{w}_h)_{\Omega_p}(s) ds \leq \int_0^t \left\| (\eta/k)^{\frac{1}{2}} \partial_t \mathbf{w}_h(s) \right\|_{\Omega_p}^2 ds + \int_0^t \left\| (k/\eta)^{\frac{1}{2}} \mathbf{g}(s) \right\|_{\Omega_p}^2 ds$$

and

$$\begin{aligned} 2 \int_0^t (\mathbf{f}, \partial_t \mathbf{u}_h)_{\Omega_p}(s) ds &\leq \frac{1}{t} \int_0^t \left\| \rho_u^{\frac{1}{2}} \partial_t \mathbf{u}_h(s) \right\|_{\Omega_p}^2 ds + t \int_0^t \left\| \rho_u^{-\frac{1}{2}} \mathbf{f}(s) \right\|_{\Omega_p}^2 ds \\ &\leq \max_{s \in [0,t]} \left\| \rho_u^{\frac{1}{2}} \partial_t \mathbf{u}_h(s) \right\|_{\Omega_p}^2 + t \int_0^t \left\| \rho_u^{-\frac{1}{2}} \mathbf{f}(s) \right\|_{\Omega_p}^2 ds. \end{aligned}$$

inserting the previous bounds into (42) and taking the maximum over $t \in [0, T]$, yields the assertion. \square

Remark 1. We observe that, proceeding as in [71, Lemma 7], it is possible to obtain a stability estimate for problem (33) requiring $\mu^{-1} \in L^\infty(\Omega_p)$ together with $\mathbf{f} \in H^1((0, T], \mathbf{L}^2(\Omega_p))$ instead of $\rho_u^{-1} \in L^\infty(\Omega_p)$. The key step is based on estimating the term $\int_0^t (\mathbf{f}, \partial_t \mathbf{u}_h)_{\Omega_p}$ by using partial integration and the discrete Korn's first inequality [72, Lemma 1].

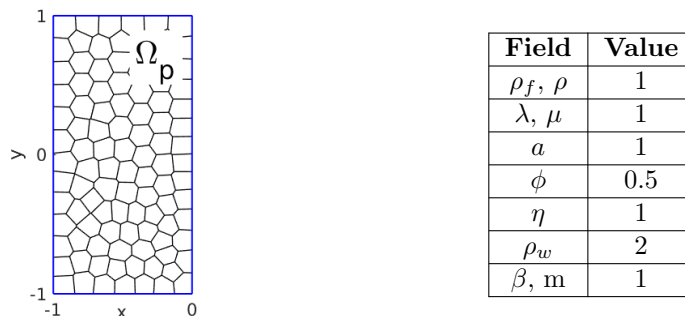


Fig. 5: Test case of Section 5.3. (Left) Poro-elastic test case. Polygonal mesh, with $N_{el} = 100$ polygons. (Right) Poro-elastic test case. Physical parameters.

For the sake of conciseness, we decide not to present here the convergence analysis for the PolydG formulation of the poro-elastic problem (33). However, an error estimate can be readily deduced from Theorem 58 below, in the case in which the exact solution on the acoustic part of the domain is null.

5.3 Verification test

We consider problem (30) in $\Omega_p = (-1, 0) \times (0, 1)$ and choose as exact solution

$$\mathbf{u}(x, y; t) = \begin{pmatrix} x^2 \cos(\frac{\pi x}{2}) \sin(\pi x) \\ x^2 \cos(\frac{\pi x}{2}) \sin(\pi x) \end{pmatrix} \cos(\sqrt{2}\pi t), \quad \mathbf{w}(x, y; t) = -\mathbf{u}(x, y; t). \quad (43)$$

As before, Dirichlet boundary conditions and initial conditions are set accordingly. The model problem is solved on a sequence of polygonal meshes as the one shown in Figure 5 (left), with physical parameters shown in Figure 5 (right).

The final time T has been set equal to 0.25, considering a timestep of $\Delta t = 10^{-4}$ for the Newmark- β scheme, $\gamma_N = 1/2$ and $\beta_N = 1/4$, cf. (17). The penalty parameters σ_0 and m_0 appearing in definitions (23) and (35), respectively, have been chosen equal to 10.

In Figure 6 (left) we report the computed \mathbf{L}^2 -errors for the elastic \mathbf{u} and filtration \mathbf{w} displacements as a function of the polynomial degree p in a semilog-scale. We fix the number of polygonal elements as $N_{el} = 100$. We observe an exponential rate of convergence since the solution (43) is analytic. In Figure 6 (right) we report the computed energy error $\|(\mathbf{u} - \mathbf{u}_h, \mathbf{w} - \mathbf{w}_h)\|_{\mathbb{E}}$, cf. (58), as a function of the mesh size h for a polynomial degree $p = 2, 3, 4$. In this case we retrieve the rate of convergence $\mathcal{O}(h^p)$ as it is proved in (58).

6 Poro-elastic-acoustic media

In this section, we present the PolydG discretization of the poro-elasto-acoustic interface problem. We refer the reader to [49] for the rigorous mathematical analysis of the model problem and the detailed derivation of the proposed

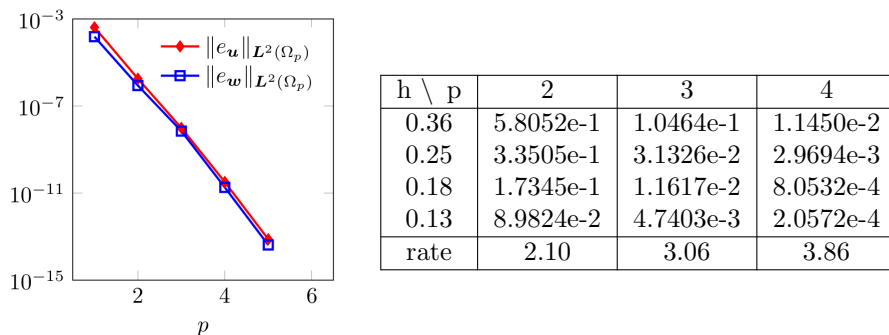


Fig. 6: Test case of Section 5.3. (Left) Computed L^2 -errors $\|e_{\mathbf{u}}\|_{L^2(\Omega_p)} = \|\mathbf{u} - \mathbf{u}_h\|_{L^2(\Omega_p)}$ and $\|e_{\mathbf{w}}\|_{L^2(\Omega_p)} = \|\mathbf{w} - \mathbf{w}_h\|_{L^2(\Omega_p)}$ as a function of the polynomial degree p in a semilogarithmic scale for $N_{el} = 100$ polygonal elements. (Right) Computed energy error as a function of the mesh size h for polynomial degree $p = 2, 3, 4$. The rate of convergence is also reported in the last row, cf. (58).

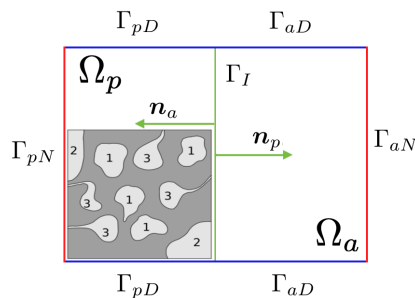


Fig. 7: Simplified representation of the domain $\Omega = \Omega_p \cup \Omega_a$ for $d = 2$. Pores classification in Ω_p : *sealed* (1), *open* (2) and *imperfect* (3).

method. In what follows, we assume that Ω is decomposed into two disjoint, polygonal/polyhedral subdomains: $\Omega = \Omega_p \cup \Omega_a$, cf. Figure 7.

The two subdomains share part of their boundary, resulting in the interface $\Gamma_I = \partial\Omega_p \cap \partial\Omega_a$. We set $\partial\Omega_p = \Gamma_{pD} \cup \Gamma_{pN} \cup \Gamma_I$ and $\partial\Omega_a = \Gamma_{aD} \cup \Gamma_{aN} \cup \Gamma_I$, where the surface measures of Γ_{pD} , Γ_{aD} , and Γ_I are assumed to be strictly positive. The outer unit normal vectors to $\partial\Omega_p$ and $\partial\Omega_a$ are denoted by \mathbf{n}_p and \mathbf{n}_a , respectively, so that $\mathbf{n}_p = -\mathbf{n}_a$ on Γ_I .

The subdomain Ω_p represents a poro-elasto medium whose dynamical behavior is described by Biot's equations (30). In the fluid domain Ω_a , we consider an acoustic wave with constant velocity $c > 0$ and mass density $\rho_a > 0$ such that $\rho_a, c^{-2} \in L^\infty(\Omega_a)$. For a given source term $h \in L^\infty((0, T]; L^2(\Omega_a))$, the

acoustic potential φ satisfies

$$\begin{cases} \rho_a c^{-2} \partial_{tt} \varphi - \nabla \cdot (\rho_a \nabla \varphi) = h & \text{in } \Omega_a \times (0, T], \\ \varphi = 0 & \text{on } \Gamma_{aD} \times (0, T], \\ \rho_a \nabla \varphi \cdot \mathbf{n}_a = 0 & \text{on } \Gamma_{aN} \times (0, T], \\ (\varphi, \partial_t \varphi) = (\varphi_0, \varphi_1) & \text{in } \Omega_a \times \{0\}, \end{cases} \quad (44)$$

with $(\varphi_0, \varphi_1) \in H_0^1(\Omega_a) \times L^2(\Omega_a)$. To close the coupled poro-elasto-acoustic problem, some interface conditions on Γ_I are needed. Here, we consider physically consistent transmission conditions (see, e.g., [22] and [73]) expressing the continuity of normal stresses, continuity of pressure, and conservation of mass:

$$\begin{cases} -\tilde{\boldsymbol{\sigma}} \mathbf{n}_p = \rho_a \dot{\varphi} \mathbf{n}_p & \text{on } \Gamma_I \times (0, T], \\ (\tau - 1) \dot{\mathbf{w}} \cdot \mathbf{n}_p + \tau p = \tau \rho_a \dot{\varphi} & \text{on } \Gamma_I \times (0, T], \\ -(\dot{\mathbf{u}} + \dot{\mathbf{w}}) \cdot \mathbf{n}_p = \nabla \varphi \cdot \mathbf{n}_p & \text{on } \Gamma_I \times (0, T]. \end{cases} \quad (45)$$

The parameter $\tau : \Gamma_I \rightarrow [0, 1]$ denotes the hydraulic permeability at the interface and models different pores configurations, cf. Figure 7. In the *open pores* region $\tau^{-1}(1) \subset \Gamma_I$ the second equation in (45) reduces to $p = \rho_a \dot{\varphi}$, while in the *sealed pores* subset $\tau^{-1}(0)$ we have $\dot{\mathbf{w}} \cdot \mathbf{n}_p = 0$, implying that $\tau^{-1}(0)$ is impermeable. Finally, the *imperfect pores* region $\tau^{-1}((0, 1))$ models an intermediate state between *open* and *sealed pores*. For later use, we split the interface into two disjoint (possibly non-connected) subsets $\Gamma_I = \Gamma_I^s \cup \Gamma_I^o$, with

$$\Gamma_I^s = \tau^{-1}(0) \quad \text{and} \quad \Gamma_I^o = \tau^{-1}((0, 1]) = \Gamma_I \setminus \Gamma_I^s.$$

We remark that the first and second conditions in (45) plays the role of a Neumann and a Robin-like conditions for system (30), respectively. Similarly, the third equation in (45) acts as a Neumann condition for problem (44). The existence and uniqueness of a strong solution to the poro-elasto-acoustic problem coupling equations (30), (44), and (45) is proved in [49, Appendix A].

In order to derive the weak formulation of the coupled problem, we introduce the function $\zeta_\tau : \Gamma_I^o \rightarrow \mathbb{R}^+$, defined by $\zeta_\tau = \tau^{-1}(1 - \tau)$, and the weighted space

$$\mathbf{W}_\tau = \{ \mathbf{z} \in \mathbf{H}_0(\text{div}, \Omega_p) \mid \zeta_\tau^{\frac{1}{2}} (\mathbf{z} \cdot \mathbf{n}_p)|_{\Gamma_I^o} \in L^2(\Gamma_I^o), (\mathbf{z} \cdot \mathbf{n}_p)|_{\Gamma_I^s} = 0 \}, \quad (46)$$

equipped with the norm

$$\| \mathbf{z} \|_{\mathbf{W}_\tau} = \| \mathbf{z} \|_{\Omega_p} + \| \nabla \cdot \mathbf{z} \|_{\Omega_p} + \| \zeta_\tau^{\frac{1}{2}} \mathbf{z} \cdot \mathbf{n}_p \|_{\Gamma_I^o} \quad \forall \mathbf{z} \in \mathbf{W}_\tau.$$

The weak form of the problem obtained by coupling equations (30), (44), and (45) reads as: for any $t \in (0, T]$, find $(\mathbf{u}, \mathbf{w}, \varphi)(t) \in \mathbf{H}_0^1(\Omega_p) \times \mathbf{W}_\tau \times H_0^1(\Omega_a)$ s.t.

$$\begin{aligned} & \mathcal{M}((\partial_{tt} \mathbf{u}, \partial_{tt} \mathbf{w}, \partial_{tt} \varphi), (\mathbf{v}, \mathbf{z}, \psi)) + \mathcal{A}((\mathbf{u}, \mathbf{w}, \varphi), (\mathbf{v}, \mathbf{z}, \psi)) + \mathcal{B}(\partial_t \mathbf{w}, \mathbf{z}) \\ & + \mathcal{C}(\partial_t \varphi, \mathbf{v} + \mathbf{z}) - \mathcal{C}(\partial_t (\mathbf{u} + \mathbf{w}), \psi) = (\mathbf{f}, \mathbf{v})_{\Omega_p} + (\mathbf{g}, \mathbf{z})_{\Omega_p} + (h, \psi)_{\Omega_a} \end{aligned} \quad (47)$$

for all $(\mathbf{v}, \mathbf{z}, \psi) \in \mathbf{H}_0^1(\Omega_p) \times \mathbf{W}_\tau \times H_0^1(\Omega_a)$, where we have set

$$\begin{aligned} \mathcal{M}((\mathbf{u}, \mathbf{w}, \varphi), (\mathbf{v}, \mathbf{z}, \psi)) &= \mathcal{M}^p((\mathbf{u}, \mathbf{w}), (\mathbf{v}, \mathbf{z})) + (\rho_a c^{-2} \varphi, \psi)_{\Omega_a}, \\ \mathcal{A}((\mathbf{u}, \mathbf{w}, \varphi), (\mathbf{v}, \mathbf{z}, \psi)) &= \mathcal{A}^e(\mathbf{u}, \mathbf{v}) + \mathcal{A}^p(\beta \mathbf{u} + \mathbf{w}, \beta \mathbf{v} + \mathbf{z}) + \mathcal{A}^a(\varphi, \psi), \\ \mathcal{B}(\mathbf{w}, \mathbf{z}) &= (\eta k^{-1} \mathbf{w}, \mathbf{z})_{\Omega_p} + (\zeta_\tau \mathbf{w} \cdot \mathbf{n}_p, \mathbf{z} \cdot \mathbf{n}_p)_{\Gamma_I^o}, \\ \mathcal{C}(\varphi, \mathbf{z}) &= \langle \rho_a \varphi, \mathbf{z} \cdot \mathbf{n}_p \rangle_{\Gamma_I}, \end{aligned} \quad (48)$$

with $\mathcal{M}^p, \mathcal{A}^e, \mathcal{A}^p$ defined in (32), (20), and (34), respectively. In (48), the bilinear form \mathcal{A}^a is defined such that $\mathcal{A}^a(\varphi, \psi) = (\rho_a \nabla \varphi, \nabla \psi)_{\Omega_a}$ for all $\varphi, \psi \in H_0^1(\Omega_a)$ and $\langle \cdot, \cdot \rangle_{\Gamma_I}$ denotes the $H^{\frac{1}{2}}(\Gamma_I) - H^{-\frac{1}{2}}(\Gamma_I)$ duality product.

6.1 Semi-discrete formulation

We decompose the polytopic regular mesh \mathcal{T}_h as $\mathcal{T}_h = \mathcal{T}_h^p \cup \mathcal{T}_h^a$, where \mathcal{T}_h^a and \mathcal{T}_h^p are aligned with Ω_a and Ω_p , respectively. In a similar way, we decompose \mathcal{F}_h as $\mathcal{F}_h = \mathcal{F}_h^I \cup \mathcal{F}_h^p \cup \mathcal{F}_h^a$, where $\mathcal{F}_h^I = \{F \in \mathcal{F}_h : F \subset \partial \kappa^p \cap \partial \kappa^a, \kappa^p \in \mathcal{T}_h^p, \kappa^a \in \mathcal{T}_h^a\}$, and \mathcal{F}_h^p and \mathcal{F}_h^a denote the faces of \mathcal{T}_h^p and \mathcal{T}_h^a , respectively, not laying on Γ_I . The discrete spaces are selected as follows: given element-wise constant polynomial degrees $p_h : \mathcal{T}_h^p \rightarrow \mathbb{N}^*$ and $r_h : \mathcal{T}_h^a \rightarrow \mathbb{N}^*$, we let $\mathbf{V}_h^p = [\mathcal{P}_{p_h}(\mathcal{T}_h^p)]^d$ and $V_h^a = \mathcal{P}_{r_h}(\mathcal{T}_h^a)$. Finally, we also assume that the coefficients ρ_a and c are piecewise constant over \mathcal{T}_h^a and τ is piecewise constant over \mathcal{F}_h^I . Under this assumption, we can decompose the set of mesh faces belonging to Γ_I as $\mathcal{F}_h^I = \mathcal{F}_h^{Is} \cup \mathcal{F}_h^{Io}$, with $\mathcal{F}_h^{Is} = \{F \in \mathcal{F}_h^I \mid F \subset \Gamma_I^s\}$ and $\mathcal{F}_h^{Io} = \mathcal{F}_h^I \setminus \mathcal{F}_h^{Is}$.

The semi-discrete PolydG formulation of problem (47) consists in finding, for all $t \in (0, T]$, the discrete solution $(\mathbf{u}_h, \mathbf{w}_h, \varphi_h)(t) \in \mathbf{V}_h^p \times \mathbf{V}_h^p \times V_h^a$ such that

$$\begin{aligned} \partial_{tt} \mathcal{M}((\mathbf{u}_h, \mathbf{w}_h, \varphi_h), (\mathbf{v}_h, \mathbf{z}_h, \psi_h)) + \mathcal{A}_h((\mathbf{u}_h, \mathbf{w}_h, \varphi_h), (\mathbf{v}_h, \mathbf{z}_h, \psi_h)) + \partial_t \mathcal{B}(\mathbf{w}_h, \mathbf{z}_h) \\ + \partial_t [\mathcal{C}_h(\varphi_h, \mathbf{v}_h + \mathbf{z}_h) - \mathcal{C}_h(\mathbf{u}_h + \mathbf{w}_h, \psi_h)] = (\mathbf{f}, \mathbf{v}_h)_{\Omega_p} + (\mathbf{g}, \mathbf{z}_h)_{\Omega_p} + (h, \psi_h)_{\Omega_a} \end{aligned} \quad (49)$$

for all discrete functions $(\mathbf{v}_h, \mathbf{z}_h, \psi_h) \in \mathbf{V}_h^p \times \mathbf{V}_h^p \times V_h^a$. As initial conditions we take the L^2 -orthogonal projections onto $(\mathbf{V}_h^p \times \mathbf{V}_h^p \times V_h^a)^2$ of the initial data $(\mathbf{u}_0, \mathbf{w}_0, \varphi_0, \mathbf{u}_1, \mathbf{w}_1, \varphi_1)$. For all $\mathbf{u}, \mathbf{v}, \mathbf{w}, \mathbf{z} \in \mathbf{V}_h^p$ and $\varphi, \psi \in V_h^a$, the bilinear forms \mathcal{A}_h and \mathcal{C}_h appearing in (49) are given by

$$\mathcal{A}_h((\mathbf{u}, \mathbf{v}, \varphi), (\mathbf{v}, \mathbf{z}, \psi)) = \mathcal{A}_h^e(\mathbf{u}, \mathbf{v}) + \tilde{\mathcal{A}}_h^p(\beta \mathbf{u} + \mathbf{w}, \beta \mathbf{v} + \mathbf{z}) + \mathcal{A}_h^a(\varphi, \psi), \quad (50)$$

$$\mathcal{C}_h(\varphi, \mathbf{v}) = (\rho_a \varphi, \mathbf{v} \cdot \mathbf{n}_p)_{\mathcal{F}_h^I}, \quad (51)$$

with $\mathcal{A}_h^e : \mathbf{V}_h^p \times \mathbf{V}_h^p \rightarrow \mathbb{R}$ defined as in (22) and

$$\begin{aligned} \tilde{\mathcal{A}}_h^p(\mathbf{w}, \mathbf{z}) &= (m \nabla \cdot \mathbf{w}, \nabla \cdot \mathbf{z})_{\mathcal{T}_h^p} - (\{m(\nabla \cdot \mathbf{w})\}, \llbracket \mathbf{z} \rrbracket \mathbf{n})_{\mathcal{F}_h^{pi} \cup \mathcal{F}_h^{pD} \cup \mathcal{F}_h^{Is}} \\ &\quad - (\llbracket \mathbf{w} \rrbracket \mathbf{n}, \{m(\nabla \cdot \mathbf{z})\})_{\mathcal{F}_h^{pi} \cup \mathcal{F}_h^{pD} \cup \mathcal{F}_h^{Is}} + (\gamma \llbracket \mathbf{w} \rrbracket \mathbf{n}, \llbracket \mathbf{z} \rrbracket \mathbf{n})_{\mathcal{F}_h^{pi} \cup \mathcal{F}_h^{pD} \cup \mathcal{F}_h^{Is}}, \\ \mathcal{A}_h^a(\varphi, \psi) &= (\rho_a \nabla \varphi, \nabla \psi)_{\mathcal{T}_h^a} - (\{\rho_a \nabla \varphi\}, \llbracket \psi \rrbracket)_{\mathcal{F}_h^{ai} \cup \mathcal{F}_h^{aD}} \\ &\quad - (\llbracket \varphi \rrbracket, \{\rho_a \nabla \psi\})_{\mathcal{F}_h^{ai} \cup \mathcal{F}_h^{aD}} + (\chi \llbracket \varphi \rrbracket, \llbracket \psi \rrbracket)_{\mathcal{F}_h^{ai} \cup \mathcal{F}_h^{aD}}. \end{aligned} \quad (52)$$

Notice that the bilinear form $\tilde{\mathcal{A}}_h^p$ is different from \mathcal{A}_h^p defined in (34). Indeed, the definition of $\tilde{\mathcal{A}}_h^p$ in (52) also takes into account the essential condition $\mathbf{z} \cdot \mathbf{n}_p = 0$ on Γ_I^s embedded in the definition of the functional space \mathbf{W}_τ . The stabilization function $\chi \in L^\infty(\mathcal{F}_h^a)$ is defined such that

$$\chi = \rho_0 \begin{cases} \max_{\kappa \in \{\kappa_1, \kappa_2\}} ((\rho_a)_{|\kappa} r_\kappa^2 h_\kappa^{-1}), & F \in \mathcal{F}_h^{ai}, F \subset \partial\kappa_1 \cap \partial\kappa_2, \\ (\rho_a)_{|\kappa} r_\kappa^2 h_\kappa^{-1}, & F \in \mathcal{F}_h^{aD}, F \subset \partial\kappa \cap \Gamma_{aD}, \end{cases} \quad (53)$$

with $\rho_0 > 0$ being a user-dependent parameter.

Denoting by (U, W, Φ) the vector of the coefficients of $(\mathbf{u}_h, \mathbf{w}_h, \varphi_h)$ in the chosen basis for $\mathbf{V}_h^p \times \mathbf{V}_h^p \times V_h^a$, the algebraic form of problem (49) reads:

$$\begin{aligned} \begin{bmatrix} \mathbf{M}_\rho^p & \mathbf{M}_{\rho_f}^p & 0 \\ \mathbf{M}_{\rho_f}^p & \mathbf{M}_{\rho_w}^p & 0 \\ 0 & 0 & M_{\rho_a c^{-2}}^a \end{bmatrix} \begin{bmatrix} \ddot{U} \\ \ddot{W} \\ \ddot{\Phi} \end{bmatrix} + \begin{bmatrix} 0 & 0 & \mathbf{C} \\ 0 & \mathbf{B} & \mathbf{C} \\ -\mathbf{C} & -\mathbf{C} & 0 \end{bmatrix} \begin{bmatrix} \dot{U} \\ \dot{W} \\ \dot{\Phi} \end{bmatrix} \\ + \begin{bmatrix} \mathbf{A}^e + \tilde{\mathbf{A}}_{\beta^2}^p & \tilde{\mathbf{A}}_\beta^p & 0 \\ \tilde{\mathbf{A}}_\beta^p & \tilde{\mathbf{A}}^p & 0 \\ 0 & 0 & \mathbf{A}^a \end{bmatrix} \begin{bmatrix} U \\ W \\ \Phi \end{bmatrix} = \begin{bmatrix} \mathbf{F} \\ \mathbf{G} \\ \mathbf{H} \end{bmatrix}, \quad (54) \end{aligned}$$

with initial data $(U, W, \Phi)(0) = (U_0, W_0, \Phi_0)$ and $(\dot{U}, \dot{W}, \dot{\Phi})(0) = (U_1, W_1, \Phi_1)$.

6.2 Stability and convergence results

In this section, we present the main stability and convergence results proved in [49]. First, we introduce the energy norm defined such that, for all $(\mathbf{u}, \mathbf{w}, \varphi) \in C^1([0, T]; \mathbf{V}_h^p \times \mathbf{V}_h^p \times V_h^a)$,

$$\begin{aligned} \|(\mathbf{u}, \mathbf{w}, \varphi)(t)\|_{\mathbb{E}}^2 &= \|(\mathbf{u}, \mathbf{w})(t)\|_{\mathcal{E}}^2 + \|\rho_a^{\frac{1}{2}} c^{-1} \partial_t \varphi(t)\|_{\Omega_a}^2 + \|\varphi(t)\|_{\text{DG}, a}^2 \\ &\quad + \|\gamma^{\frac{1}{2}} \mathbf{w} \cdot \mathbf{n}\|_{\mathcal{F}_h^{Is}}^2 + \int_0^t \|\zeta_\tau^{\frac{1}{2}} \partial_t (\mathbf{w} \cdot \mathbf{n})\|_{\mathcal{F}_h^{Io}}^2 ds, \quad (55) \end{aligned}$$

with $\|\cdot\|_{\mathcal{E}}$ defined in (37) and $\|\cdot\|_{\text{DG}, a} : \mathbf{V}_h^a \rightarrow \mathbb{R}^+$ given by

$$\|\varphi\|_{\text{DG}, a}^2 = \|\rho_a^{\frac{1}{2}} \nabla \varphi\|_{\mathcal{T}_h^a}^2 + \|\chi^{\frac{1}{2}} [\![\varphi]\!] \|_{\mathcal{F}_h^{aI} \cup \mathcal{F}_h^{aD}}^2 \quad \forall \varphi \in \mathbf{V}_h^a \oplus H_0^1(\Omega_a). \quad (56)$$

The stability of the semi-discrete PolydG problem (49) is a consequence of Proposition 6.1 below, which also implies that the formulation is dissipative. Indeed, in the case of null external source terms, it follows from estimate (57) that $\|(\mathbf{u}_h, \mathbf{w}_h, \varphi_h)(t)\|_{\mathbb{E}} \lesssim \|(\mathbf{u}_h, \mathbf{w}_h, \varphi_h)(0)\|_{\mathbb{E}}$ for any $t > 0$. The proof of the following result is based on taking $(\mathbf{v}_h, \mathbf{z}_h, \psi_h) = (\partial_t \mathbf{u}_h, \partial_t \mathbf{w}_h, \partial_t \varphi_h) \in \mathbf{V}_h^p \times \mathbf{V}_h^p \times V_h^a$ in (49), using the skew-symmetry of the coupling terms, and then reasoning as in Proposition 5.1 (see [49, Theorem 3.4] for the details).

Proposition 6.1. *For sufficiently large penalty parameters σ_0, m_0, ρ_0 and for any $t \in (0, T]$, the solution $(\mathbf{u}_h, \mathbf{w}_h, \varphi_h)(t) \in \mathbf{V}_h^p \times \mathbf{V}_h^p \times V_h^a$ of (49) satisfies*

$$\|(\mathbf{u}_h, \mathbf{w}_h, \varphi_h)(t)\|_{\mathbb{E}} \lesssim \|(\mathbf{u}_h, \mathbf{w}_h, \varphi_h)(0)\|_{\mathbb{E}} + \int_0^t \|\mathbf{f}(s)\|_{\Omega_p}^2 + \|\mathbf{g}(s)\|_{\Omega_p}^2 + \|h(s)\|_{\Omega_a}^2 ds, \quad (57)$$

with hidden constant depending on time t and on the material properties, but independent of the interface parameter τ .

In what follows, we report the main result concerning the error analysis of the PolydG discretization (49). To infer the error estimate of Theorem 6.1 below, an additional assumption on the interface permeability τ is required.

Assumption 6.1. *For each $F \in \mathcal{F}_h^{I\circ}$ and $\kappa \in \mathcal{T}_h^p$ such that $F \subset \partial\kappa \cap \Gamma_I^\circ$, it holds $(\zeta_\tau)|_F = (\frac{1-\tau}{\tau})|_F \lesssim \frac{p_\kappa^2}{h_\kappa}$, with hidden constant independent of τ .*

We remark that the previous assumption is used only for establishing the error estimate below but, according to our observation, it is not needed in practical applications. We refer the reader to [49, Theorem 4.3] for the detailed proof of the following result.

Theorem 6.1. *Let Assumption 3.1, Assumption 3.2, and Assumption 6.1 be satisfied and assume that the solution $(\mathbf{u}, \mathbf{w}, \varphi)$ of the weak formulation (31) is sufficiently regular. For any time $t \in [0, T]$, let $(\mathbf{u}_h, \mathbf{w}_h, \varphi_h)(t) \in \mathbf{V}_h^p \times \mathbf{V}_h^p \times V_h^a$ be the PolydG solution of problem (49) obtained with sufficiently large penalization parameters σ_0, m_0 and ρ_0 . Then, for any time $t \in (0, T]$, the discretization error $\mathbf{E}(t) = (\mathbf{u} - \mathbf{u}_h, \mathbf{w} - \mathbf{w}_h, \varphi - \varphi_h)(t)$ satisfies*

$$\begin{aligned} \|\mathbf{E}(t)\|_{\mathbb{E}} \lesssim & \sum_{\kappa \in \mathcal{T}_h^p} \frac{h_\kappa^{s_\kappa-1}}{p_\kappa^{m_\kappa-3/2}} \left(\mathcal{I}_{m_\kappa}^{\mathcal{T}_\sharp}(\mathbf{u}, \mathbf{w})(t) + \int_0^t \mathcal{I}_{m_\kappa}^{\mathcal{T}_\sharp}(\partial_t \mathbf{u}, \partial_t \mathbf{w})(s) ds \right) \\ & + \sum_{\kappa \in \mathcal{T}_h^a} \frac{h_\kappa^{q_\kappa-1}}{r_\kappa^{l_\kappa-3/2}} \left(\mathcal{I}_{l_\kappa}^{\mathcal{T}_\sharp}(\varphi)(t) + \int_0^t \mathcal{I}_{l_\kappa}^{\mathcal{T}_\sharp}(\partial_t \varphi)(s) ds \right), \end{aligned} \quad (58)$$

where

$$\begin{aligned} \mathcal{I}_{m_\kappa}^{\mathcal{T}_\sharp}(\mathbf{u}, \mathbf{w}) &= \|\tilde{\mathcal{E}}\mathbf{u}\|_{\mathbf{H}^{m_\kappa}(\mathcal{T}_\sharp)} + \|\tilde{\mathcal{E}}\mathbf{w}\|_{\mathbf{H}^{m_\kappa}(\mathcal{T}_\sharp)} + \|\tilde{\mathcal{E}}\partial_t \mathbf{u}\|_{\mathbf{H}^{m_\kappa}(\mathcal{T}_\sharp)} + \|\tilde{\mathcal{E}}\partial_t \mathbf{w}\|_{\mathbf{H}^{m_\kappa}(\mathcal{T}_\sharp)}, \\ \mathcal{I}_{l_\kappa}^{\mathcal{T}_\sharp}(\varphi) &= \|\tilde{\mathcal{E}}\varphi\|_{H^{l_\kappa}(\mathcal{T}_\sharp)} + \|\tilde{\mathcal{E}}\partial_t \varphi\|_{H^{l_\kappa}(\mathcal{T}_\sharp)}, \end{aligned}$$

with $s_\kappa = \min(p_\kappa + 1, m_\kappa)$ and $q_\kappa = \min(r_\kappa + 1, l_\kappa)$ for all $\kappa \in \mathcal{T}_h$. The hidden constant depends on time t , the material properties, and the shape-regularity of the covering \mathcal{T}_\sharp , but is independent of the discretization parameters and of τ .

6.3 Verification test

As a verification test case we study the poro-elasto-acoustic problem (30),(44) with (45) conditions in $\Omega = \Omega_p \cup \Omega_a = (-1, 1) \times (0, 1)$. We consider a sequence

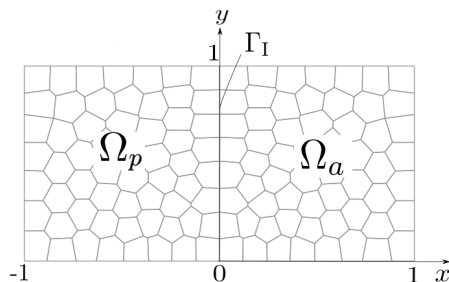


Fig. 8: Test case of Section 6.3. Polygonal mesh with $N_{el} = 100$ elements.

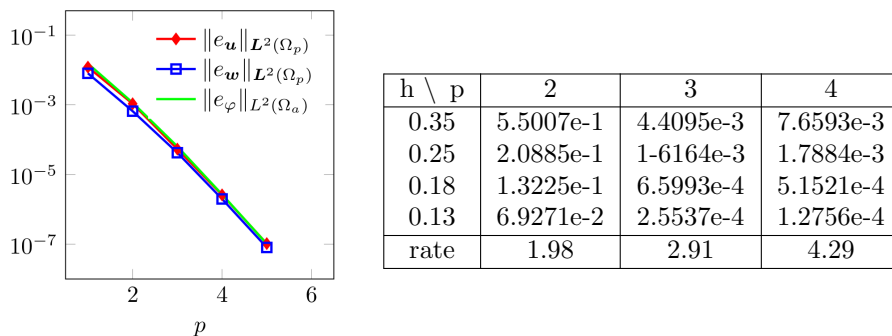


Fig. 9: Test case of Section 6.3. (Left) Computed L^2 -errors $\|e_{\mathbf{u}}\|_{L^2(\Omega_p)} = \|\mathbf{u} - \mathbf{u}_h\|_{L^2(\Omega_p)}$, $\|e_{\mathbf{w}}\|_{L^2(\Omega_p)} = \|\mathbf{w} - \mathbf{w}_h\|_{L^2(\Omega_p)}$ and $\|e_{\varphi}\|_{L^2(\Omega_a)} = \|\varphi - \varphi_h\|_{L^2(\Omega_a)}$ as a function of the polynomial degree p in a semilogarithmic scale with by fixing the number of polygonal elements as $N_{el} = 100$. (Right) Computed energy error as a function of the mesh size h for polynomial degree $p = 2, 3, 4$. The rate of convergence is also reported in the last row, cf. (58).

of polygonal meshes as the one shown in Figure 8, the physical parameters listed in Figure 5 (right) and $c = \rho_a = 1$. As exact solution we consider (43) in Ω_p and

$$\varphi(x, y; t) = x^2 \sin(\pi x) \sin(\pi y) \sin(\sqrt{2}\pi t),$$

in Ω_a in order to have a null pressure in the whole poroelastic domain. Dirichlet and initial conditions are set accordingly. We remark that with this choice the interface coupling conditions are null on Γ_I . For the following test cases we consider $\tau = 1$ (open pores) at the interface, however similar results can be obtained with $\tau \in [0, 1)$, cf. [49]. We fix the $T = 0.25$ and consider a time step $\Delta t = 10^{-4}$ for the Newmark- β scheme, $\gamma_N = 1/2$ and $\beta_N = 1/4$, cf. (17). Penalty parameters σ_0 and m_0 in Ω_p as well as $\rho_0 \in \Omega_a$ are set equal to 10, cf. (23), (35) and (53), respectively.

Finally, in Figure 9 (left) we report in a semilog-scale the computed L^2 -norms of the error fixing a computational mesh of $N_{el} = 100$ polygons and varying

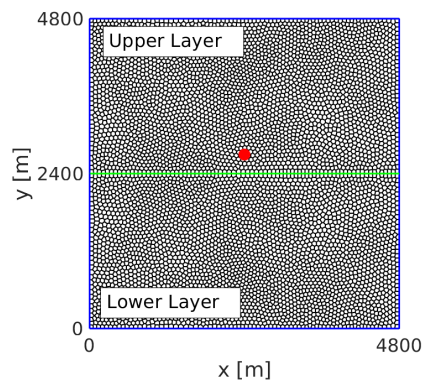


Fig. 10: Test case of Section 7.1. Computational domain: the location of the point-source force is superimposed in red.

the polynomial degree $p = 1, 2, \dots, 5$. An exponential decay of the error is clearly attained. In Figure 9 (right) we report the computed energy errors as a function of the mesh-size h , for the $p = 2, 3, 4$. Consistently with (58) the errors decay proportionally to h^p .

7 Examples of physical interest

7.1 Two layered media

In this section we consider a wave propagation problem in heterogeneous media taken from [29]. The aim of this test is to show how different assumptions on the model can determine and change the behavior of the wave propagation. The domain of interest is $\Omega = (0, 4.8)^2$ km² and consists of two layers as depicted in Figure 10. In the first case (a) the layers are perfectly elastic, cf. Table 1, while in the second case (b) the layers are assumed to be poro-elastic, cf. Table 2. A point-wise source \mathbf{f} , cf. (11), acting in the y -direction is located in the upper part of the domain at point $\mathbf{x} = (2.4, 2.7)$ km. The time evolution of the latter is given by a Ricker-wavelet (12) with amplitude $A_0 = 1$ m, time-shift $t_0 = 0.3$ s and peak-frequency $f_p = 5$ Hz. For both models (a) and (b) we use a shape-polygonal mesh with characteristic size $h = 100$ and a polynomial degree $p = 3$. We set homogeneous Dirichlet conditions on the boundary and use null initial conditions. To integrate in time model (a) we chose the leap-frog scheme while for model (b) the Newmark- β scheme with parameters β and γ as in the previous section. We fix the final time $T = 1$ s and chose $\Delta t = 1.e - 3$ s.

In Figure 11 we report some snapshots of the computed magnitude of the velocity field $|\mathbf{v}|$ for models (a) and (b). As expected, the propagation of the wave in the elastic domain is regular and refraction phenomena are not very evident (due to a low contrast between the wave speeds). On the contrary, when porous media are accounted for, the refraction effects are more pronounced. This

		Lower Layer	Upper Layer	
Solid density	ρ	2650	2200	kg/m ³
Shear modulus	μ	1.5038 · 10 ⁹	4.3738 · 10 ⁹	Pa
Lamé coefficient	λ	1.8121 · 10 ⁹	7.2073 · 10 ⁹	Pa
Damping coefficient	ζ	0	0	s ⁻¹

Tab. 1: Test case of Section 7.1. Physical parameters for elastic media.

			Lower Layer	Upper Layer	
Fluid	Fluid density	ρ_f	750	950	kg/m ³
	Dynamic viscosity	η	0	0	Pa · s
Grain	Solid density	ρ_s	2650	2200	kg/m ³
	Shear modulus	μ	1.5038 · 10 ⁹	4.3738 · 10 ⁹	Pa
Matrix	Porosity	ϕ	0.2	0.4	
	Tortuosity	a	2	2	
	Permeability	k	1 · 10 ⁻¹²	1 · 10 ⁻¹²	m ²
	Lamé coefficient	λ	1.8121 · 10 ⁹	7.2073 · 10 ⁹	Pa
	Biot's coefficient	m	7.2642 · 10 ⁹	6.8386 · 10 ⁹	Pa
	Biot's coefficient	β	0.9405	0.0290	

Tab. 2: Test case of Section 7.1. Physical parameters for poro-elastic media.

is in agreement with the findings in [29].

7.2 Wave propagation in layered poro-elastic-acoustic media

As a final test cases we consider the domain reproduced in Figure 12 where an acoustic layer is in contact with a heterogeneous poro-elastic body.

For the acoustic domain we set $\rho_a = 1500$ [kg/m³] and $c = 1000$ [m/s]. Physical parameters for the poro-elastic domain are chosen as in Table 2 where, for this case, the property of the former “Lower Layer” are assigned to the first poro-elastic subdomain, while those of the former “Upper Layer” to the second poro-elastic subdomain, cf. Figure 12. In this numerical example we chose the dynamic viscosity η equal to 0.001. Boundary and initial conditions have been set equal to zero both for the poroelastic and the acoustic domain. Forcing terms are null in Ω_p , while in Ω_a we consider a force of the form $h = r(x, y)q(t)$, where q is a Ricker wavelet of the form (12) with $A_0 = 1$ [Hz m³], $\beta_p = 39.4784$ [Hz²] and $t_0 = 0.75$ s. The function $r(x, y)$ is defined as $r(x, y) = 1$, if $(x, y) \in \bigcup_{i=1}^4 B(\mathbf{x}_i, R)$, while $r(x, y) = 0$, otherwise, where $B(\mathbf{x}_i, R)$ is the circle centered in \mathbf{x}_i and with radius R . Here, we set $\mathbf{x}_1 = (13097, 8868)$ m, $\mathbf{x}_2 = (16673, 8868)$ m, $\mathbf{x}_3 = (27079, 8868)$ m, $\mathbf{x}_4 = (29324, 8868)$ m and $R = 100$ m. Notice that, the support of the function $r(x, y)$ has been reported in Figure 12, superimposed with a sample of the computational mesh employed.

Simulations have been carried out by considering: a polygonal mesh consisting in $N = 6356$ triangles, subdivided into $N_a = 2380$ and $N_p = 3976$ triangles

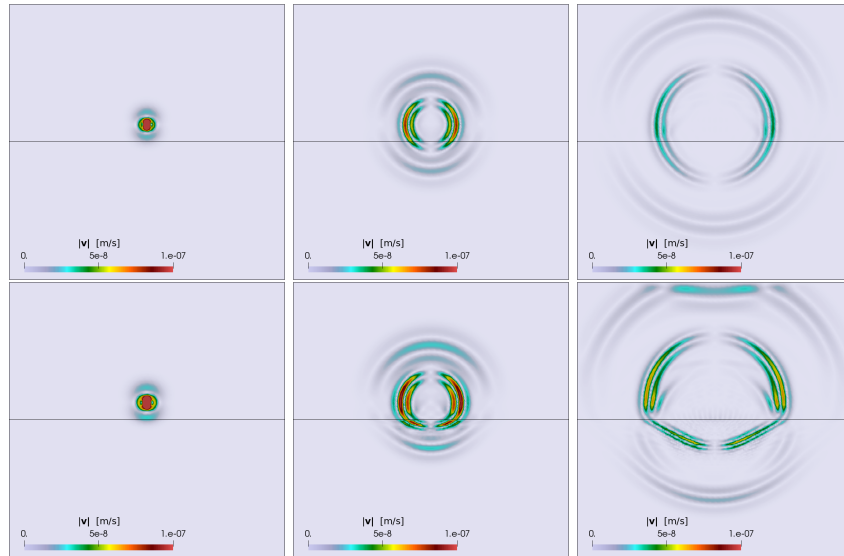


Fig. 11: Test case of Section 7.1. Computed velocity field $|\mathbf{v}|$ at the time instants $t = 0.3$ s (left), $t = 0.6$ s (center) and $t = 1$ s (right) for elastic model (a) (top) and poro-elastic model (b) (bottom).

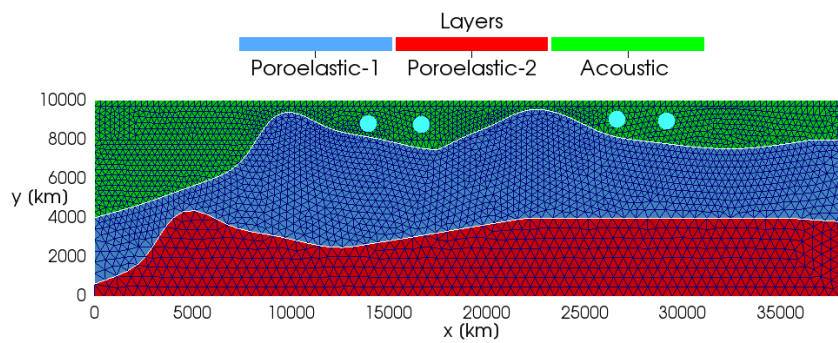


Fig. 12: Test case of Section 7.2. Computational domain. Location of the acoustic sources are also superimposed.

for the acoustic and poroelastic domain, respectively; a Newmark scheme with time step $\Delta t = 10^{-2}$ s and $\gamma_N = 1/2$ and $\beta_N = 1/4$ in a time interval $[0, 4]$ s; a polynomial degree $p_\kappa = r_\kappa = p = 4$. In Figure 13, we show the computed pressure p_h considering the interface permeability $\tau = 1$. The latter value models an *open* pores condition at the interface, cf. (45). Remark that $p_h = \rho_a \dot{\varphi}_h$ in the acoustic domain while $p_h = -m(\beta \nabla \cdot \mathbf{u}_h + \nabla \cdot \mathbf{w}_h)$ in the poro-elastic one. As one can see, the pressure wave correctly propagates from the acoustic domain to the poro-elastic one: the continuity at the interface boundary can be appreciated. Finally, we note how the second porous layer (sound absorbing material) produces a damping of the pressure field.

8 Conclusions

In this work we have presented a review of the development of PolyDG methods for multiphysics wave propagation problem in elastic, poro-elastic and poro-elasto-acoustic media.

After having recalled the theoretical background of the analysis of PolyDG methods we analysed the well-posedness and stability of different numerical formulations and proved hp-version a priori error estimates for the semi-discrete scheme. Time integration of the latter is obtained based on employing the leap-frog or the a Newmark-scheme. Numerical experiments have been designed not only to verify the numerical performance of PolyDG methods but also to exploit the flexibility in the process of mesh design offered by polytopic elements. In this respect, numerical tests of physical interest have been also discussed.

To conclude, we can affirm that PolyDG methods allow a robust and flexible numerical discretization that can be successfully applied to wave propagation problems. Future developments in this direction include the study of multiphysics problems such as fluid-structure (with poro-elastic or thermo-elastic structure) interaction problems as well as the exploitation of agglomeration-based algorithms to design multilevel and multigrid methods for the efficient iterative solution of the (linear) system of equations stemming from the PolyDG discretization.

References

- [1] S. Triebenbacher, M. Kaltenbacher, B. Wohlmuth, and B. Flemisch. Applications of the mortar finite element method in vibroacoustics and flow induced noise computations. *Acta Acust. united Ac.*, 96(3):536–553(18), 2010.
- [2] B. Krishnan, M. Divyadev, S. Raja, and K. Venkataramana. Structural and Vibroacoustic Analysis of Aircraft Fuselage Section with Passive Noise Reducing Materials: A Material Performance Study. In *IES*, 03 2015.
- [3] B. Castagnede, A. Aknine, M. Melon, and C. Depollier. Ultrasonic char-

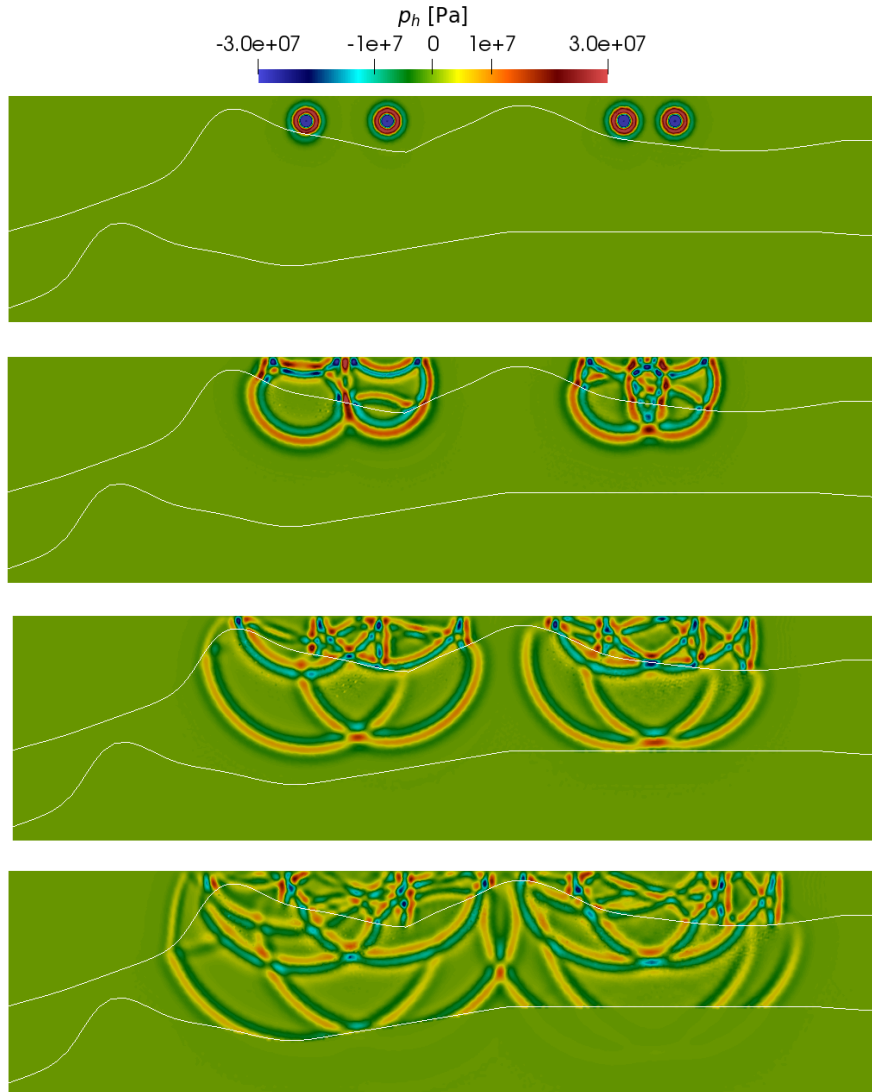


Fig. 13: Test case of Section 7.2. Computed pressure p_h in the poro-elastic-acoustic domain at four time instants (from up to down $t = 1, 2, 3, 3.8$ s), with $\Delta t = 10^{-2}$ s.

- acterization of the anisotropic behavior of air-saturated porous materials. *Ultrasonics*, 36(1-5):323–341, 1998.
- [4] T. J. Haire and C. M. Langton. Biot theory: a review of its application to ultrasound propagation through cancellous bone. *Bone*, 24(4):291 – 295, 1999.
- [5] J. M. Carcione. *Wave Fields in Real Media (Third Edition)*, volume 38. Elsevier Science, Oxford, 2014.
- [6] E. Chaljub, E. Maufroy, P. Moczo, J. Kristek, F. Hollender, P.-Y. Bard, E. Priolo, P. Klin, F. de Martin, Z. Zhang, W. Zhang, and X. Chen. 3-D numerical simulations of earthquake ground motion in sedimentary basins: testing accuracy through stringent models. *Geophys. J. Int.*, 201(1):90–111, 2015.
- [7] A. Pitarka, A. Akinici, P. De Gori, and M. Buttinelli. Deterministic 3D Ground-Motion Simulations (0–5 Hz) and Surface Topography Effects of the 30 October 2016 Mw 6.5 Norcia, Italy, Earthquake. *B. Seismol. Soc. Am.*, 2021.
- [8] D. McCallen, A. Petersson, A. Rodgers, A. Pitarka, M. Miah, F. Petrone, B. Sjogreen, N. Abrahamson, and H. Tang. EQSIM—a multidisciplinary framework for fault-to-structure earthquake simulations on exascale computers part i: Computational models and workflow. *Earthq. Spectra*, 37(2):707–735, 2021.
- [9] J. Bielak, O. Ghattas, and E.-J. Kim. Parallel octree-based finite element method for large-scale earthquake ground motion simulation. *Comput. Model. Eng. Sci.*, 10(2):99–112, 2005.
- [10] M. Dumbser, M. Käser, and E. F. Toro. An arbitrary high-order Discontinuous Galerkin method for elastic waves on unstructured meshes-V. Local time stepping and p -adaptivity. *Geophys. J. Int.*, 171(2):695–717, 2007.
- [11] C. Pelties, J. Puente, J.-P. Ampuero, G.B. Brietzke, and M. Käser. Three-dimensional dynamic rupture simulation with a high-order discontinuous Galerkin method on unstructured tetrahedral meshes. *J. Geophys. Res. Solid Earth*, 117(B2), 2012.
- [12] K. Duru, L. Rannabauer, A.-A. Gabriel, G. Kreiss, and M. Bader. A stable discontinuous Galerkin method for the perfectly matched layer for elastodynamics in first order form. *Numer. Math.*, 146(4):729–782, 2020.
- [13] A. Breuer, A. Heinecke, and Y. Cui. EDGE: Extreme scale fused seismic simulations with the discontinuous Galerkin method. In *International Supercomputing Conference*, pages 41–60. Springer, 2017.

-
- [14] D. Komatitsch, Q. Liu, J. Tromp, P. Suss, C. Stidham, and J. H. Shaw. Simulations of ground motion in the Los Angeles basin based upon the spectral-element method. *B. Seismol. Soc. Am.*, 94(1):187–206, 2004.
- [15] M. Stupazzini, R. Paolucci, and H. Igel. Near-fault earthquake ground-motion simulation in the Grenoble valley by a high-performance spectral element code. *B. Seismol. Soc. Am.*, 99(1):286–301, 2009.
- [16] P. Galvez, J.-P. Ampuero, L. A. Dalguer, S. N. Somala, and T. Nissen-Meyer. Dynamic earthquake rupture modelled with an unstructured 3-D spectral element method applied to the 2011 M9 Tohoku earthquake. *Geophys. J. Int.*, 198(2):1222–1240, 2014.
- [17] J. D. De Basabe, M. K. Sen, and M. F. Wheeler. The interior penalty discontinuous Galerkin method for elastic wave propagation: grid dispersion. *Geophys. J. Int.*, 175(1):83–93, 2008.
- [18] P. F. Antonietti, A. Ferroni, I. Mazzieri, R. Paolucci, A. Quarteroni, C. Smerzini, and M. Stupazzini. Numerical modeling of seismic waves by discontinuous spectral element methods. *ESAIM Proc. Surveys*, 61:1–37, 2018.
- [19] A. Ferroni, P. F. Antonietti, I. Mazzieri, and A. Quarteroni. Dispersion-dissipation analysis of 3-D continuous and discontinuous spectral element methods for the elastodynamics equation. *Geophys. J. Int.*, 211:1554–1574, 2017.
- [20] M. A. Biot. Theory of Propagation of Elastic Waves in a Fluid-Saturated Porous Solid. I. Low-Frequency Range. *J. Acoust. Soc. Am.*, 28:168–178, 1956.
- [21] D. M. J. Smeulders. *On wave propagation in saturated and partially saturated porous media*. PhD thesis, Citeseer, 1992.
- [22] B. Gurevich and M. Schoenberg. Interface conditions for Biot’s equations of poroelasticity. *J. Acoust. Soc. Am.*, 105(5):2585–2589, 1999.
- [23] G. Chiavassa and B. Lombard. Wave propagation across acoustic/Biot’s media: A finite-difference method. *Commun. Comput. Phys.*, 13(4):985–1012, 2013.
- [24] R. T. Rockafellar. Lagrange multipliers and optimality. *SIAM review*, 35(2):183–238, 1993.
- [25] I. Ambartsumyan, E. Khattatov, I. Yotov, and P. Zunino. A Lagrange multiplier method for a Stokes–Biot fluid–poroelastic structure interaction model. *Numer. Math.*, 140(2):513–553, 2018.
- [26] B. Flemisch, M. Kaltenbacher, and B. Wohlmuth. Elasto-acoustic and acoustic-acoustic coupling on non-matching grids. *Internat. J. Numer. Methods Engrg.*, 67:1791–1810, 2006.

-
- [27] A. Bermúdez, R. Rodríguez, and D. Santamarina. Finite element approximation of a displacement formulation for time-domain elastoacoustic vibrations. *J. Comput. Appl. Math.*, 152(1):17–34, 2003.
- [28] B. Flemisch, M. Kaltenbacher, S. Triebenbacher, and B. Wohlmuth. The equivalence of standard and mixed finite element methods in applications to elasto-acoustic interaction. *SIAM J. Sci. Comput.*, 32(4):1980–2006, 2010.
- [29] C. Morency and J. Tromp. Spectral-element simulations of wave propagation in porous media. *Geophys. J. Int.*, 175(1):301–345, 2008.
- [30] R. Sidler, J. M. Carcione, and K. Holliger. Simulation of surface waves in porous media. *Geophys. J. Int.*, 183(2):820–832, 2010.
- [31] J. de la Puente, M. Dumbser, M. Käser, and H. Igel. Discontinuous Galerkin methods for wave propagation in poroelastic media. *Geophysics*, 73(5):T77–T97, 2008.
- [32] B. Lombard and J. Piraux. Numerical treatment of two-dimensional interfaces for acoustic and elastic waves. *J. Comput. Phys.*, 195(1):90–116, 2004.
- [33] P. F. Antonietti, F. Brezzi, and L. D. Marini. Bubble stabilization of discontinuous galerkin methods. *Comput. Methods Appl. Mech. Engrg.*, 198(21-26):1651–1659, 2009.
- [34] F. Bassi, L. Botti, A. Colombo, D. A. Di Pietro, and P. Tesini. On the flexibility of agglomeration based physical space discontinuous Galerkin discretizations. *J. Comput. Phys.*, 231(1):45–65, 2012.
- [35] P. F. Antonietti, S. Giani, and P. Houston. *hp*-version composite Discontinuous Galerkin methods for elliptic problems on complicated domains. *SIAM J. Sci. Comput.*, 35(3):A1417–A1439, 2013.
- [36] A. Cangiani, E. H. Georgoulis, and P. Houston. *hp*-version discontinuous Galerkin methods on polygonal and polyhedral meshes. *Math. Models Methods Appl. Sci.*, 24(10):2009–2041, 2014.
- [37] A. Cangiani, Z. Dong, E. H. Georgoulis, and P. Houston. *hp*-version discontinuous Galerkin methods for advection-diffusion-reaction problems on polytopic meshes. *ESAIM Math. Model. Numer. Anal.*, 50(3):699–725, 2016.
- [38] S. Congreve and P. Houston. Two-grid *hp*-DGFEMs on agglomerated coarse meshes. *PAMM*, 19(1):e201900175, 2019.
- [39] A. Cangiani, P. Dong, and E. H. Georgoulis. *hp*-version discontinuous Galerkin methods on essentially arbitrarily-shaped elements, 2020.

-
- [40] A. Cangiani, Z. Dong, and E. H. Georgoulis. *hp*-version space-time discontinuous Galerkin methods for parabolic problems on prismatic meshes. *SIAM J. Sci. Comput.*, 39(4):A1251–A1279, 2017.
- [41] P. F. Antonietti, C. Facciola, A. Russo, and M. Verani. Discontinuous Galerkin Approximation of Flows in Fractured Porous Media on Polytopic Grids. *SIAM J. Sci. Comput.*, 41(1):A109–A138, 2019.
- [42] P. F. Antonietti, M. Verani, C. Vergara, and S. Zonca. Numerical solution of fluid-structure interaction problems by means of a high order Discontinuous Galerkin method on polygonal grids. *Finite Elem. Anal. Des.*, 159:1–14, 2019.
- [43] B. Rivière and M. F. Wheeler. Discontinuous finite element methods for acoustic and elastic wave problems. *Contemp. Math.*, 329:271–282, 2003.
- [44] M. J. Grote, A. Schneebeli, and D. Schötzau. Discontinuous Galerkin finite element method for the wave equation. *SIAM J. Numer. Anal.*, 44(6):2408–2431, 2006.
- [45] P. F. Antonietti and I. Mazzieri. High-order Discontinuous Galerkin methods for the elastodynamics equation on polygonal and polyhedral meshes. *Comput. Methods Appl. Mech. Engrg.*, 342:414–437, 2018.
- [46] P. F. Antonietti, I. Mazzieri, M. Muhr, V. Nikolić, and B. Wohlmuth. A high-order discontinuous Galerkin method for nonlinear sound waves. *J. Comput. Phys.*, 415:109484, 2020.
- [47] P. F. Antonietti, F. Bonaldi, and I. Mazzieri. A high-order discontinuous Galerkin approach to the elasto-acoustic problem. *Comput. Methods Appl. Mech. Engrg.*, 358:112634, 29, 2020.
- [48] P. F. Antonietti, F. Bonaldi, and I. Mazzieri. Simulation of three-dimensional elastoacoustic wave propagation based on a Discontinuous Galerkin Spectral Element Method. *Internat. J. Numer. Methods Engrg.*, 121(10):2206–2226, 2020.
- [49] P. F. Antonietti, M. Botti, I. Mazzieri, and S. Nati Poltri. A high-order discontinuous Galerkin method for the poro-elasto-acoustic problem on polygonal and polyhedral grids. *SIAM J. Sci. Comput.*, 2021. In press.
- [50] R. Kosloff and D. Kosloff. Absorbing boundaries for wave propagation problems. *J. Comput. Phys.*, 63(2):363–376, 1986.
- [51] I. B. Morozov. Geometrical attenuation, frequency dependence of Q , and the absorption band problem. *Geophys. J. Int.*, 175(1):239–252, 2008.
- [52] D. Komatitsch and J. Tromp. Spectral-element simulations of global seismic wave propagation-I. Validation. *Geophys. J. Int.*, 149(2):390–412, 2002.

-
- [53] P. Moczo, J. Kristek, and M. Gális. *The Finite-Difference Modelling of Earthquake Motions: Waves and Ruptures*. Cambridge University Press, United Kingdom, 2014.
- [54] A. Quarteroni, A. Tagliani, and E. Zampieri. Generalized Galerkin approximations of elastic waves with absorbing boundary conditions. *Comput. Methods Appl. Mech. Engrg.*, 163(1–4):323 – 341, 1998.
- [55] E. Bécache, D. Givoli, and T. Hagstrom. High-order absorbing boundary conditions for anisotropic and convective wave equations. *J. Comput. Phys.*, 229(4):1099–1129, 2010.
- [56] M. A. Biot. General theory of three-dimensional consolidation. *J. Appl. Phys.*, 12(2):155–164, 1941.
- [57] N. Ricker. The form and laws of propagation of seismic wavelets. *Geophysics*, 18:10–40, 1953.
- [58] K. F. Graff. *Wave Motion in Elastic Solids*. Courier Corporation, United States, 1975.
- [59] K. Aki and Paul G. Richards. *Quantitative seismology*, volume 1. Sausalito CA: University Science Books, United States, 2002.
- [60] E. Faccioli, F. Maggio, R. Paolucci, and A. Quarteroni. 2D and 3D elastic wave propagation by a pseudo-spectral domain decomposition method. *J. Seismol.*, 1(3):237–251, 1997.
- [61] A. Cangiani, Z. Dong, E. H. Georgoulis, and P. Houston. *hp-version discontinuous Galerkin methods on polytopic meshes*. SpringerBriefs in Mathematics. Springer International Publishing, Switzerland, 2017.
- [62] D. N. Arnold, F. Brezzi, B. Cockburn, and L. D. Marini. Unified analysis of discontinuous Galerkin methods for elliptic problems. *SIAM J. Numer. Anal.*, 39(5):1749–1779, 2001/02.
- [63] P. F. Antonietti, A. Cangiani, J. Collis, Z. Dong, E. H. Georgoulis, S. Giani, and P. Houston. Review of Discontinuous Galerkin Finite Element Methods for Partial Differential Equations on Complicated Domains. *Lect. Notes Comput. Sci. Eng.*, 114:281 – 310, 2015.
- [64] E. M. Stein. *Singular integrals and differentiability properties of functions*, volume 2. Princeton University Press, United States, 1970.
- [65] P. F. Antonietti, B. Ayuso de Dios, I. Mazzieri, and A. Quarteroni. Stability analysis of discontinuous Galerkin approximations to the elastodynamics problem. *J. Sci. Comput.*, 68:143–170, 2016.
- [66] B. Rivière, S. Shaw, and J. R. Whiteman. Discontinuous Galerkin finite element methods for dynamic linear solid viscoelasticity problems. *Numer. Methods Partial Differ. Equ.*, 23(5):1149–1166, 2007.

-
- [67] P.-A. Raviart and J.-M. Thomas. *Introduction à l'analyse numérique des équations aux dérivées partielles*. Masson, France, 1983.
- [68] P. F. Antonietti, C. Facciola, P. Houston, I. Mazzieri, G. Pennesi, and M. Verani. *High-order Discontinuous Galerkin Methods on Polyhedral Grids for Geophysical Applications: Seismic Wave Propagation and Fractured Reservoir Simulations*, pages 159–225. Springer International, 2021.
- [69] P. J. Matuszyk and L. F. Demkowicz. Solution of coupled poroelastic/acoustic/elastic wave propagation problems using automatic hp-adaptivity. *Comput. Methods Appl. Mech. Engrg.*, 281:54–80, 2014.
- [70] A. Ezziani. *Modélisation mathématique et numérique de la propagation d'ondes dans les milieux viscoélastiques et poroélastiques*. Theses, ENSTA ParisTech, 2005.
- [71] D. Boffi, M. Botti, and D. A. Di Pietro. A nonconforming high-order method for the Biot problem on general meshes. *SIAM J. Sci. Comput.*, 38(3):A1508–A1537, 2016.
- [72] M. Botti, D. A. Di Pietro, and A. Guglielmana. A low-order nonconforming method for linear elasticity on general meshes. *Comput. Methods Appl. Mech. Eng.*, 354:96–118, 2019.
- [73] G. Chiavassa and B. Lombard. Time domain numerical modeling of wave propagation in 2d heterogeneous porous media. *J. Comput. Phys.*, 230(13):5288–5309, 2011.

MOX Technical Reports, last issues

Dipartimento di Matematica
Politecnico di Milano, Via Bonardi 9 - 20133 Milano (Italy)

- 65/2021** Mazzieri, I.; Muhr, M.; Stupazzini, M.; Wohlmuth, B.
Elasto-acoustic modelling and simulation for the seismic response of structures: The case of the Tahtali dam in the 2020 Izmir earthquake
- 64/2021** Clarotto, L.; Allard, D.; Menafoglio, A.
A new class of alpha-transformations for the spatial analysis of Compositional Data
- 63/2021** Rosafalco, L.; Torzoni, M.; Manzoni, A.; Mariani, S.; Corigliano, A.
Online structural health monitoring by model order reduction and deep learning algorithms
- 62/2021** Lupo Pasini, M.; Burcul, M.; Reeve, S.; Eisenbach, M.; Perotto, S.
Fast and accurate predictions of total energy for solid solution alloys with graph convolutional neural networks
- 60/2021** Rosafalco, L.; Manzoni, A.; Mariani, S.; Corigliano, A.
Fully convolutional networks for structural health monitoring through multivariate time series classification
- 61/2021** Buchwald, S.; Ciaramella, G.; Salomon, J.; Sugny, D.
A greedy reconstruction algorithm for the identification of spin distribution
- 59/2021** Stella, S.; Regazzoni, F.; Vergara, C.; Dede', L.; Quarteroni, A.
A fast cardiac electromechanics model coupling the Eikonal and the nonlinear mechanics equations
- 58/2021** Tassi, T., Zingaro, A., Dede', L.
Enhancing numerical stabilization methods for advection dominated differential problems by Machine Learning algorithms
- 57/2021** Roberto Piersanti, Francesco Regazzoni, Matteo Salvador, Antonio F. Corno, Luca Dede', Chri
3D-0D closed-loop model for the simulation of cardiac biventricular electromechanics
- 56/2021** Zingaro, A.; Fumagalli, I.; Dede' L.; Fedele M.; Africa P.C.; Corno A.F.; Quarteroni A.
A multiscale CFD model of blood flow in the human left heart coupled with a lumped parameter model of the cardiovascular system